THE UNIVERSITY OF CHICAGO

IMPROVED MEASUREMENTS OF THE TEMPERATURE AND E-MODE
POLARIZATION OF THE CMB FROM THE FULL 500-SQUARE-DEGREE SPTPOL
DATASET

A DISSERTATION SUBMITTED TO
THE FACULTY OF THE DIVISION OF THE PHYSICAL SCIENCES
IN CANDIDACY FOR THE DEGREE OF
DOCTOR OF PHILOSOPHY

DEPARTMENT OF PHYSICS

BY
TI-LIN CHOU

CHICAGO, ILLINOIS
JUNE 2024

To God who created the universe

To my mom Yolanda Yu, and my cat Arthur

TABLE OF CONTENTS

LIST OF FIGURES

LIST OF TABLES

ACKNOWLEDGMENTS

I feel very privileged to have not just one advisor but two: Tom and Kimmy. You have helped me every step along the way of this 6-year journey, and I am very thankful for that.

I'd also like to thank everyone in the SPT collaboration; you have all helped me in various ways.

ABSTRACT

We present updated measurements of the temperature and E-mode polarization maps of the cosmic microwave background (CMB), as well as the E-mode polarization auto-power spectrum (EE) and temperature-E-mode cross-power spectrum (TE) in the angular multipole range $50 < \ell < 8000$, using the full four-year SPTpol 500 deg^2 dataset in both the 95 GHz and 150 GHz frequency bands. These are the most sensitive measurements of the CMB damping tail to date for roughly $\ell > 1700$ in TE and $\ell > 2000$ in EE. This dataset and most of its subsets are good fits to the ΛCDM model. This dataset is self-consistent but has a curiosity that persists from the previously published SPTpol TE/EE analysis. The ΛCDM parameter constraints between the $\ell < 1000$ and $\ell > 1000$ data splits are different by $\lesssim 2\sigma$, where $\ell < 1000$ prefers a low H_0 and a high $10^9 A_s e^{-2\tau}$, and $\ell > 1000$ prefers a high H_0 and a low $10^9 A_s e^{-2\tau}$. In 150 GHz, H_0 is 66.93 ± 4.64 km s^{-1} Mpc^{-1} in the $\ell < 1000$ data split, and 74.98 ± 3.73 km s^{-1} Mpc^{-1} in the $\ell > 1000$ data split. This same trend is seen in both 95 GHz data alone and 150 GHz data alone, which suggests this is a real feature on this 500 deg^2 patch of sky. We also find the degree of lensing of the CMB, inferred from the smearing of TE/EE power spectrum peaks, to be lower than unity ($A_L = 0.70 \pm 0.13$). With A_L fixed to 0.7, the ΛCDM parameter constraints agree between the 150 GHz $\ell < 1000$ and $\ell > 1000$ data splits, therefore the A_L curiosity is another way to represent the high / low-ℓ curiosity. In the base ΛCDM model, our A_s is significantly lower than *Planck*, but when we fit our data with the $\Lambda CDM + A_L$ extended model, our marginalized ΛCDM parameter constraints become consistent with *Planck*.

CHAPTER 1

INTRODUCTION

The temperature and polarization measurements of the cosmic microwave background (CMB) provide valuable information about cosmology [e.g., Hu and Dodelson, 2002, Galli et al., 2014]. Their angular power spectra are well-fit by the ΛCDM model, and currently the best constraints for most of the ΛCDM parameters come from CMB experiments, in particular the *Planck* satellite [Planck Collaboration et al., 2020], but also ground-based experiments such as the Atacama Cosmology Telescope [ACT, e.g., Aiola et al., 2020] and the South Pole Telescope [SPT, e.g., Balkenhol et al., 2023]. In recent years, tensions have emerged between some of these parameter constraints and those measured from the late-time universe [e.g, Verde et al., 2023, Heymans et al., 2021]. A possible source of these tensions could be unmodeled systematics in one or more of the CMB experiments, therefore it is helpful to study consistencies within and across these CMB datasets. In this work we focus on internal consistencies within the SPTpol 500 deg^2 dataset.

The SPT [Carlstrom et al., 2011], with its arcminute-scale resolution and polarization-sensitive detectors, probes an important space of the CMB power spectra. Specifically, the SPTpol 500 deg^2 measurements in this work cover a wide range of angular modes, from the first peak to the damping tail, in both temperature and polarization. SPTpol was the 2nd generation receiver installed on SPT, and it was composed of 1536 transition edge sensor detectors at 95 or 150 GHz. This work is an extension to Henning et al. [2018, hereafter H18], where we perform a similar TE/EE power spectrum analysis. H18 only analyzed data from the 150 GHz detectors, and only from the first three years of 500 deg^2 observations; in this work, we analyze the full four-year dataset, and we use data from both the 95 GHz and the 150 GHz frequency bands. In H18, the data used to report the entire multipole range of bandpowers were processed identically, but in this work, we process the data in two ways: a low-ℓ focused dataset and a high-ℓ focused dataset. This allows us to make the most

sensitive measurements of the CMB damping tail to date for roughly $\ell > 1700$ in TE and $\ell > 2000$ in EE. We present our 500 deg^2 temperature and E-mode polarization maps, as well as our TE and EE angular power spectra in the multipole range $50 < \ell < 8000$.

We provide an update to the mild tension between low-ℓ and high-ℓ cosmological parameter preferences found in H18. H18 had unresolved curiosities including internal tensions and poor fits to ΛCDM, some of which could be due to unmodeled systematics. In this work we cast a wider net searching for systematic effects, and we make several improvements including stringent cuts, extensive null tests, and updated beam measurements. We follow up on the aforementioned curiosities with these improved measurements of the SPTpol 500 deg^2 TE/EE power spectra.

This thesis is structured as follows. We describe the SPTpol observations and time-ordered data in Chapter 2. From this data, we make maps and present them in Chapter 3. From these maps, we make power spectra with methods described in Chapter 4, and we present the binned power spectra (bandpowers) in Chapter 5. We fit these bandpowers to cosmological models with the methods described in Chapter 6, and we present the parameter constraints in Chapter 7. We discuss the conclusions in Chapter 8.

CHAPTER 2

OBSERVATIONS AND DATA REDUCTION

The SPTpol instrument, the 500 deg^2 survey field, and the scan strategies are the same as H18; please refer to that work for more details. H18 only analyzed data from the 150 GHz detectors, and only from the first three years of observations; in this work, we analyzed the full four-year dataset, and used data from both the 95 GHz and the 150 GHz frequency bands.

2.1   Observations

Observations from April 2013 to May 2014 were made using the "lead-trail" scan strategy, where the 500 deg^2 field was split into two halves, with one half observed after the other in the same azimuth-elevation range. Observations from May 2014 to Sep 2016 were made using the "full-field" scan strategy, where we scanned across the full range of right ascension (RA) of the 500 deg^2 field. For each observation, we produce a 95 GHz map and a 150 GHz map, however one or both of them can fail during the time stream processing described in Section 2.2. Unlike H18, we do not perform observation cuts based on low-ℓ noise, but we remove ~ 200 observations based on jackknife null tests described in Section 5.1. The final number of 95 GHz observations used in this dataset is 1481 lead-trail & 3368 full-field, and the number of 150 GHz observations used in this dataset is 1481 lead-trail & 3387 full-field.

2.2   Time Stream Processing

We record the time-ordered data (time streams) of each detector, and they go through several processes before being combined into maps. As in H18, spectral lines related to the pulse tube coolers are notch-filtered; additionally, in this work the 95 GHz time streams show a strong 1 Hz noise line, so that line is also notch-filtered. To further improve signal-to-noise

at high ℓ over H18, we then analyze two copies of the time stream; we apply a high-ℓ focused set of filters on one copy, and apply a low-ℓ focused set of filters on the other copy.

For the high-ℓ focused time stream, we subtract a 5th-order (or 9th-order) Legendre polynomial on a scan-by-scan basis for lead-trail (or full-field) observations. To prevent noise at low ℓ_x from mixing into high-ℓ modes, we apply a high-pass filter at $\ell_x = 300$, and a common-mode filter that removes the average of all time streams in the same frequency band. For anti-aliasing, we apply a low-pass filter at $\ell_x = 20{,}000$.

For the low-ℓ focused time stream, we first downsample the data by a factor of 2, and then subtract the same 5th-order (or 9th-order) Legendre polynomial for lead-trail (or full-field) observations. This step effectively equals a high-pass filter at $\ell_x \sim 50$, and we apply no further high-pass filters. For anti-aliasing, we apply a low-pass filter at $\ell_x = 3{,}200$.

Both copies of the time stream go through the same cross-talk removal, detector data cuts, and pre-map calibration as H18, except we make one additional detector cut on the high-ℓ focused time stream data due to a noise line. Detectors with anomalously high noise in the 8–11 Hz frequency band are cut on a per-observation basis.

CHAPTER 3

MAPS

We combine time streams into flat-sky T, Q, U maps in the same way as H18. For the high-ℓ focused time stream, we use square $0.5'$ pixels, and for the low-ℓ focused time stream, we use square $3'$ pixels to speed up computations. From these low-ℓ focused maps only, we remove a scan-synchronous structure that we call "RA stripes". (We find that the average pixel value as a function of RA is not consistent with zero, therefore we take the $1°$-smoothed version of it as the template, and subtract it off from all maps.) To correct for monopole T-to-P leakage (see Section 4.6), we subtract a scaled copy of the T map from the Q and U maps, and then we construct the E-mode polarization map from Q and U in the same way as H18 [Zaldarriaga, 2001].

Figure 3.1 shows the 150 GHz total coadd of the low-ℓ focused maps, and the 150 GHz and 95 GHz noise maps, for temperature and E-mode polarization. Figure 3.2 shows the noise spectra of these various types of maps. The white noise level in the multipole range $5000 < \ell \leq 6000$ is 5.9 μK-arcmin for the 150 GHz temperature map, 8.4 μK-arcmin for the 150 GHz E-mode map, 13.5 μK-arcmin for the 95 GHz temperature map, and 19.2 μK-arcmin for the 95 GHz E-mode map.

Similar to H18, we make 50 partial coadds (map bundles) for lead-trail and full-field separately, where each bundle is constructed to have 1/50th of the total T map weights. Each lead-trail bundle is then coadded with a full-field bundle in chronological order, and these 50 "lead-trail plus full-field" map bundles will be used in Section 4.1 to calculate the angular power spectra. In total, we have 50 map bundles for 150 GHz and 50 for 95 GHz, where each bundle has a T map and an E map. Lastly, we make noise map realizations by randomly separating all the ~ 4800 maps into two subsets, coadding each subset, and subtracting these two half-depth coadded maps. We do all of this for the low-ℓ focused maps and the high-ℓ focused maps separately.
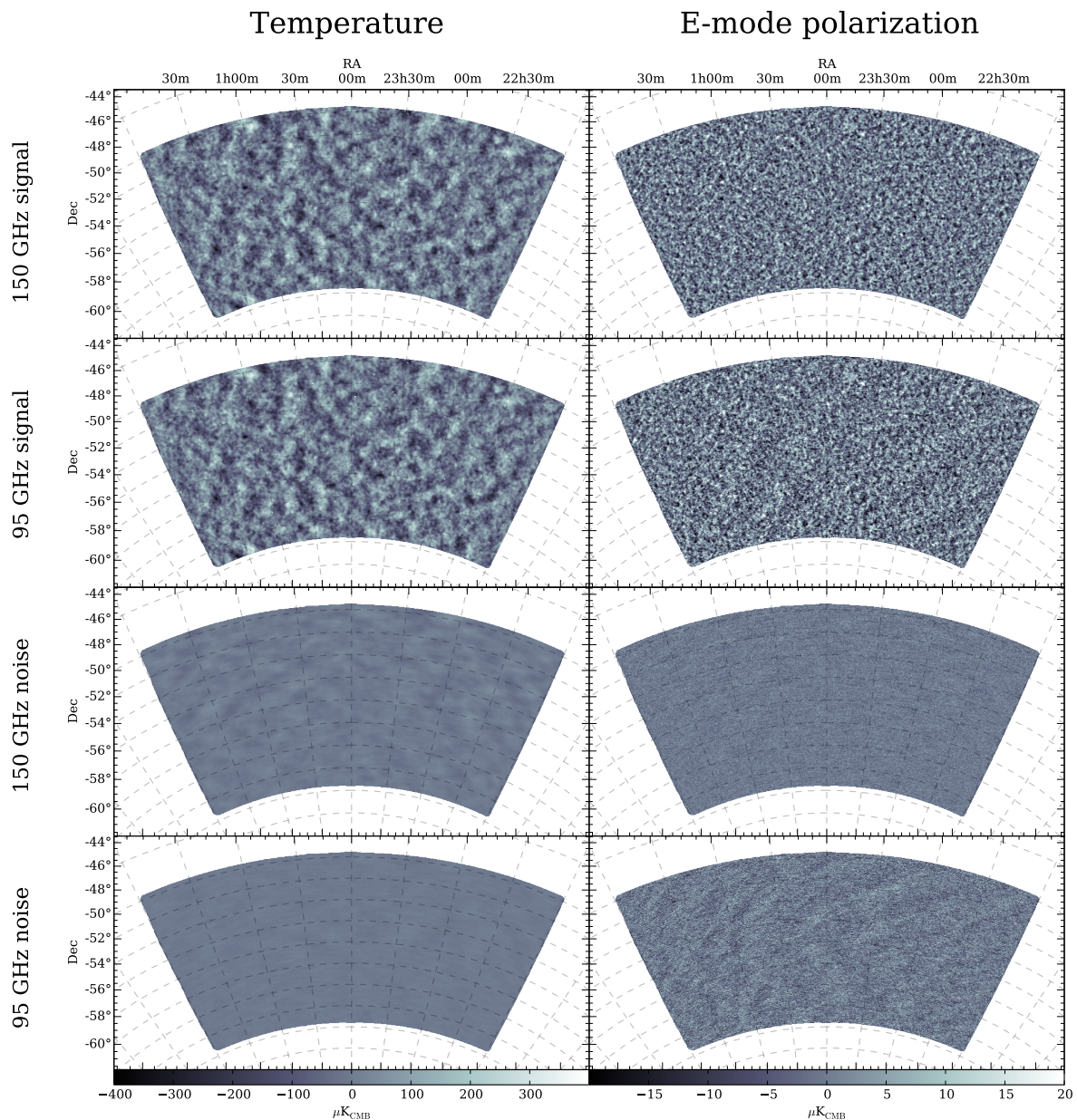
Figure 3.1: SPTpol 500 deg^2 low-ℓ focused signal and noise maps, for 150 GHz and 95 GHz, for temperature and E-mode polarization. The noise maps are made with the coadd of left-going scans minus the coadd of right-going scans, then divided by 2.
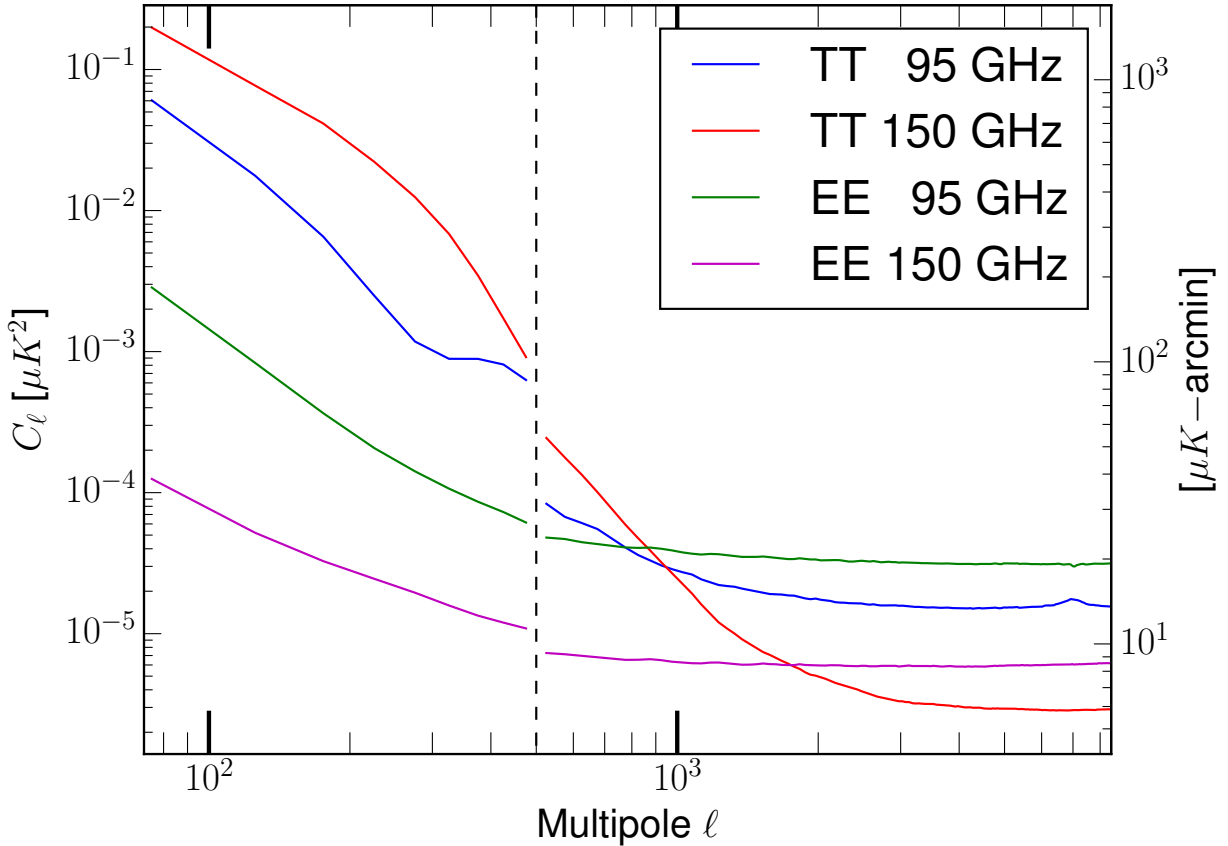
Figure 3.2: SPTpol 500 deg^2 noise spectra. For $\ell < 500$, we use the low-ℓ focused dataset; for $\ell > 500$, we use the high-ℓ focused dataset, and the dashed line at $\ell = 500$ shows this stitch. These are unbiased spectra but multiplied by the beam function again (B_ℓ^2) to show the white noise level. The axis on the left is in units of μK^2, while the axis on the right is in units of μK-arcmin. As the figure shows, the high-ℓ focused dataset has a lower noise level, because the aggressive highpass filter prevents contamination from atmospheric noise and 1/f noise.

CHAPTER 4

POWER SPECTRUM

4.1   Pseudo Cross-Spectra

We compute angular power spectra with the same pseudo-spectrum method as H18 [Hivon et al., 2002], using cross-spectra to avoid noise bias [Polenta et al., 2005, Tristram et al., 2005, Lueker et al., 2010]. From among our 50 map bundles in 150 GHz and 50 bundles in 95 GHz, we compute cross-spectra of every possible pair, never crossing the same bundle with itself. We compute all seven possible TE or EE cross-spectra ($95T \times 95E$, $95T \times 150E$, $150T \times 95E$, $150T \times 150E$, $95E \times 95E$, $95E \times 150E$, $150E \times 150E$), and take the average within each type. We do these for the low-ℓ focused maps and the high-ℓ focused maps separately.

These cross-spectra are computed at a native ℓ resolution of $\Delta\ell = 5$. We denote them as $\widetilde{C}_\lambda$, where λ represents the resolution of $\Delta\ell = 5$, and the tilde above indicates that these are pseudo-spectra. The pseudo-spectrum can be represented as the result of a biasing kernel K acting on the unbiased power spectrum [Hivon et al., 2002]; equivalently, the unbiased power spectrum equals the inverse of the biasing kernel acting on the pseudo-spectrum, and we perform this inverse after binning to a resolution of $\Delta\ell = 50$. In Einstein summation notation,

$$
\widetilde{C}_\beta = K_{\beta\beta'} C_{\beta'}
$$
$$
\Rightarrow C_\beta = K^{-1}_{\beta\beta'} \widetilde{C}_{\beta'}
$$
$$
= K^{-1}_{\beta\beta'} P_{\beta'\lambda} \widetilde{C}_\lambda \tag{4.1}
$$

where β denotes a resolution of $\Delta\ell = 50$, and $P_{\beta\lambda}$ is defined as a binning operator that bins bandpowers from a resolution of λ into a resolution of β. The biasing kernel K consists of

the mode-coupling matrix M due to the apodization mask, the filter transfer function F, and the beam function B:

$$K_{\lambda\lambda'} = M_{\lambda\lambda'}F_{\lambda'}B_{\lambda'}^2 \tag{4.2}$$

In the next three sections, we will discuss these three components in more detail. They are computed at a native resolution of $\Delta\ell = 5$, and then the biasing kernel is binned to $\Delta\ell = 50$:

$$K_{\beta\beta'} = P_{\beta\lambda}K_{\lambda\lambda'}Q_{\lambda'\beta'} \tag{4.3}$$

where $Q_{\lambda\beta}$ is the reciprocal to the binning operator $P_{\beta\lambda}$. After obtaining the unbiased cross-spectra C_β, we convert them to D_β using the operator $S_{\beta\beta} = \dfrac{\ell^{(\beta)}(\ell^{(\beta)} + 1)}{2\pi}$ where $\ell^{(\beta)}$ is the ℓ center of bin β. Finally, we coarse-bin them into increasingly wider ℓ bins starting at $\ell \geq 2000$, in order to reduce the total number of bandpowers and simplify numerical computations.

$$D_b = P_{b\beta}S_{\beta\beta}C_\beta \tag{4.4}$$

These final ℓ bins and D_b are shown in Chapter 5, and they are used in Chapter 6 for fitting cosmological parameters. In addition, we also compute unbiased noise spectra from the noise map realizations mentioned in the previous chapter, and they will be used in the construction of the bandpower covariance matrix in Section 5.2.

4.2 Mask and Mode-Coupling

We make our apodization and point source mask in the same way as H18, where all point sources with unpolarized flux > 50 mJy at 95 or 150 GHz are masked. We also compute the mode-coupling matrix $M_{\lambda\lambda'}$ analytically, in the same way as H18. The mode-coupling

9

matrices in this work and in H18 both exhibit band-diagonal structures, where elements the same distance away from the diagonal are approximately equal, therefore we average them together during the construction of the bandpower covariance matrix in Section 5.2. We do these for the low-ℓ focused maps and the high-ℓ focused maps separately.

4.3 Transfer Function

The filter transfer function F accounts for the effects of time stream processing described in Section 2.2. As in H18, we solve for it using simulated skies and "mock-observations." We make 226 realizations of the sky from a given CMB power spectrum C_ℓ, where C_ℓ is the best-fit theory to the *Planck* `base_plikHM_TT_lowTEB_lensing` dataset [Planck Collaboration et al., 2020]. Next, we add a realization of the foreground power to each sky realization. The foreground power spectrum is modeled as follows:

$$\text{foreground } D_\ell^{TT} = (A_{\text{src}}^{\text{dusty}} + A_{\text{src}}^{\text{radio}})(\frac{\ell}{3000})^2 + A_{\text{CIB}}(\frac{\ell}{3000})^{0.8} + A_{\text{tSZ}} \cdot \text{template}$$

$$\text{foreground } D_\ell^{EE} = (A_{\text{src}}^{\text{dusty}} p^{\text{dusty}} + A_{\text{src}}^{\text{radio}} p^{\text{radio}})(\frac{\ell}{3000})^2 + A_{\text{dust}}^{EE}(\frac{\ell}{80})^{-0.42}$$

where the mean-squared polarization fraction for dusty point sources $p^{\text{dusty}} = 0.0004$, for radio point sources $p^{\text{radio}} = 0.0014$, and the tSZ model template is taken from Shaw et al. [2010]. For 150 GHz, the amplitudes in μK^2 are: $\{A_{\text{src}}^{\text{dusty}} = 9, A_{\text{src}}^{\text{radio}} = 10, A_{\text{CIB}} = 3.46, A_{\text{tSZ}} = 4, A_{\text{dust}}^{EE} = 0.0236\}$. For 95 GHz, the amplitudes in μK^2 are: $\{A_{\text{src}}^{\text{dusty}} = 1.5, A_{\text{src}}^{\text{radio}} = 50, A_{\text{CIB}} = 0.56, A_{\text{tSZ}} = 12, A_{\text{dust}}^{EE} = 0.00338\}$.

We convolve these sky realizations with the beam function B_ℓ, which is different for 95 GHz and 150 GHz. Next, we mock-observe these sky realizations by scanning through them at the same telescope pointings as recorded in each of our ~ 4800 observations. Time stream processing, map-making and bundling are also done in the same way as real data, and the end product is 226 simulated datasets: We have all the low-ℓ focused and high-ℓ focused

map bundles, for 95 or 150 GHz, for each sky realization.

We compute the auto-spectrum of the coadd map for each sky realization. We do this separately for $95T \times 95T$, $150T \times 150T$, $95E \times 95E$, and $150E \times 150E$. These are pseudo-spectra, and the input theory C_ℓ^{TT} and C_ℓ^{EE} are known, so we solve for the filter transfer functions iteratively as in H18 [Hivon et al., 2002]. For the six types of TT or EE spectra above, we compute their transfer functions one at a time by plugging in the average $\widetilde{C}_\lambda$ of 226 simulations and $C_{\lambda,th}$: (again, λ denotes a resolution of $\Delta\ell = 5$)

$$
F_{\lambda,1} = \frac{\langle \widetilde{C}_\lambda \rangle}{w_2 C_{\lambda,th} B_\lambda^2}
$$

$$
F_{\lambda,i+1} = F_{\lambda,i} + \frac{M_{\lambda\lambda'} F_{\lambda',i} C_{\lambda',th} B_{\lambda'}^2}{w_2 C_{\lambda,th} B_\lambda^2}
$$

where w_2 denotes the second moment of the apodization mask. This method could be numerically unstable for TE spectra due to their zero-crossings, therefore we define the TE transfer functions as the geometric mean of the corresponding TT and EE transfer functions:

$$
F_\lambda^{95T \times 95E} = \sqrt{F_\lambda^{95T \times 95T} \cdot F_\lambda^{95E \times 95E}}
$$

$$
F_\lambda^{95T \times 150E} = \sqrt{F_\lambda^{95T \times 95T} \cdot F_\lambda^{150E \times 150E}}
$$

$$
F_\lambda^{150T \times 95E} = \sqrt{F_\lambda^{150T \times 150T} \cdot F_\lambda^{95E \times 95E}}
$$

$$
F_\lambda^{150T \times 150E} = \sqrt{F_\lambda^{150T \times 150T} \cdot F_\lambda^{150E \times 150E}}
$$

These transfer functions F_λ are used in unbiasing our bandpowers as described in Section 4.1. For later use, we also unbias these simulated spectra $\widetilde{C}_\lambda$ using the same method. In addition, we repeat the above simulation process but with an "alternate" cosmology instead of *Planck*, and they will be used in the pipeline consistency tests (Section 6.3). We do all of this for the low-ℓ focused maps and the high-ℓ focused maps separately.

4.4 Beam and Calibration

We use Venus observations to estimate the beam function B_ℓ of our instrument. For 150 GHz, we use the same observations as H18. For 95 GHz we find map artifacts in these Venus observations, but their angular power lies far above ℓ of 8000; our 95 GHz Mars maps do not have these artifacts, and our Venus beam is indeed consistent with our Mars beam, so we continue to use these Venus maps for better sensitivity at low ℓ. (See Appendix A for details.)

Pointing error (jitter) is negligible for these planet observations, but for CMB field scans, it causes the effective beam size to increase. We estimate this by fitting 2D Gaussians to the brightest point sources in the 500 deg^2 field. For 150(95) GHz, the final size of the Gaussian beam is $1.22'(1.90')$ FWHM. We convolve each Venus map with a 2D Gaussian whose FWHM is the quadrature difference between $1.22'$ (or $1.90'$) and the size of Venus in that map. For 95 GHz and 150 GHz separately, we take the cross-spectra between these maps, and their average is our B_ℓ^2.

While computing these beam functions, we discovered that B_ℓ at $\ell < 800$ can vary greatly depending on our Venus mapmaking options. This low-ℓ beam uncertainty can be well described by a one-parameter model $B_\ell \rightarrow B_\ell + A_{\text{beam}} \cdot \Delta B_\ell$ where ΔB_ℓ is a known vector describing the typical shape of this variation, and A_{beam} is a free parameter of its amplitude. For the case of 150 GHz, we fit for A_{beam} and the temperature calibration factor T_{cal} at the same time against *Planck*. As in H18, we mock-observe the *Planck* 143 GHz temperature map in the same way as our observations, and take its cross-spectrum with the SPTpol 150 GHz temperature map:

$$T_{\text{cal}}^{\text{S150}}(B_\ell^{\text{S150}} + A_{\text{beam}}^{\text{S150}} \cdot \Delta B_\ell^{\text{S150}}) = \sqrt{F_\ell^P} B_\ell^P \frac{\langle \text{Re}[\text{fmap}_1^{*,\text{S150}} \cdot \text{fmap}_2^{\text{S150}}]\rangle_\ell}{\langle \text{Re}[\text{fmap}^{*,P} \cdot \text{fmap}^{\text{S150}}]\rangle_\ell} \tag{4.5}$$

where the superscript P denotes *Planck* 143 GHz, S150 denotes SPTpol 150 GHz, fmap denotes the temperature map in Fourier space, and the subscripts in fmap_1 or fmap_2 denote two independent half-depth maps of SPTpol 150 GHz. We compute the right hand side with uncertainties, then perform a least-squares fit over the range $100 < \ell < 1000$. Under the best-fit $T_{\text{cal}}^{\text{S150}}$ and $A_{\text{beam}}^{\text{S150}}$ values, Figure 4.1 shows what we now define as the "fiducial" B_ℓ^{S150}, and for illustration purposes, we also show the range of $\Delta B_\ell^{\text{S150}}$ that corresponds to 1-σ uncertainties in the $A_{\text{beam}}^{\text{S150}}$ parameter. For the case of 95 GHz, we similarly fit for A_{beam} and T_{cal} at the same time against 150GHz:

$$T_{\text{cal}}^{\text{S95}}(B_\ell^{\text{S95}} + A_{\text{beam}}^{\text{S95}} \cdot \Delta B_\ell^{\text{S95}}) = T_{\text{cal}}^{\text{S150}} \cdot \text{fiducial } B_\ell^{\text{S150}} \cdot \frac{\langle \text{Re}[\text{fmap}_i^{*,\text{S95}} \cdot \text{fmap}_j^{\text{S150}}]\rangle_{i \neq j,\ell}}{\langle \text{Re}[\text{fmap}_i^{*,\text{S150}} \cdot \text{fmap}_j^{\text{S150}}]\rangle_{i \neq j,\ell}}$$

where S95 denotes SPTpol 95 GHz, and the subscripts i, j denote the i-th or j-th map bundle. We similarly define the fiducial B_ℓ^{S95} using the best-fit values of $T_{\text{cal}}^{\text{S95}}$ and $A_{\text{beam}}^{\text{S95}}$. For the polarization calibration factor P_{cal}, we repeat the above process using E-mode polarization maps instead of temperature maps. We adopt the value $P_{\text{cal}}^{S150} = 1.06$ found in H18, and in this work we find $P_{\text{cal}}^{S95} = 1.043$. When performing cosmology fits, we still allow these $T_{\text{cal}}, P_{\text{cal}}$, and beam uncertainty parameters to float as nuisance parameters, with their 1-σ uncertainty ranges as priors (Section 6.2).

4.5   Bandpower Window Functions

To compare theory spectra C_l^{th} with our bandpowers D_b, we need to find the bandpower window functions that convert C_l^{th} to the equivalent D_b^{th}. First off, the pseudo-spectra $\widetilde{C}^{th}$ equals the biasing kernel K acting on the theory C_l^{th} (binned),

$$\widetilde{C}_\lambda^{th} = K_{\lambda\lambda'}P_{\lambda'l}C_l^{th}$$

13
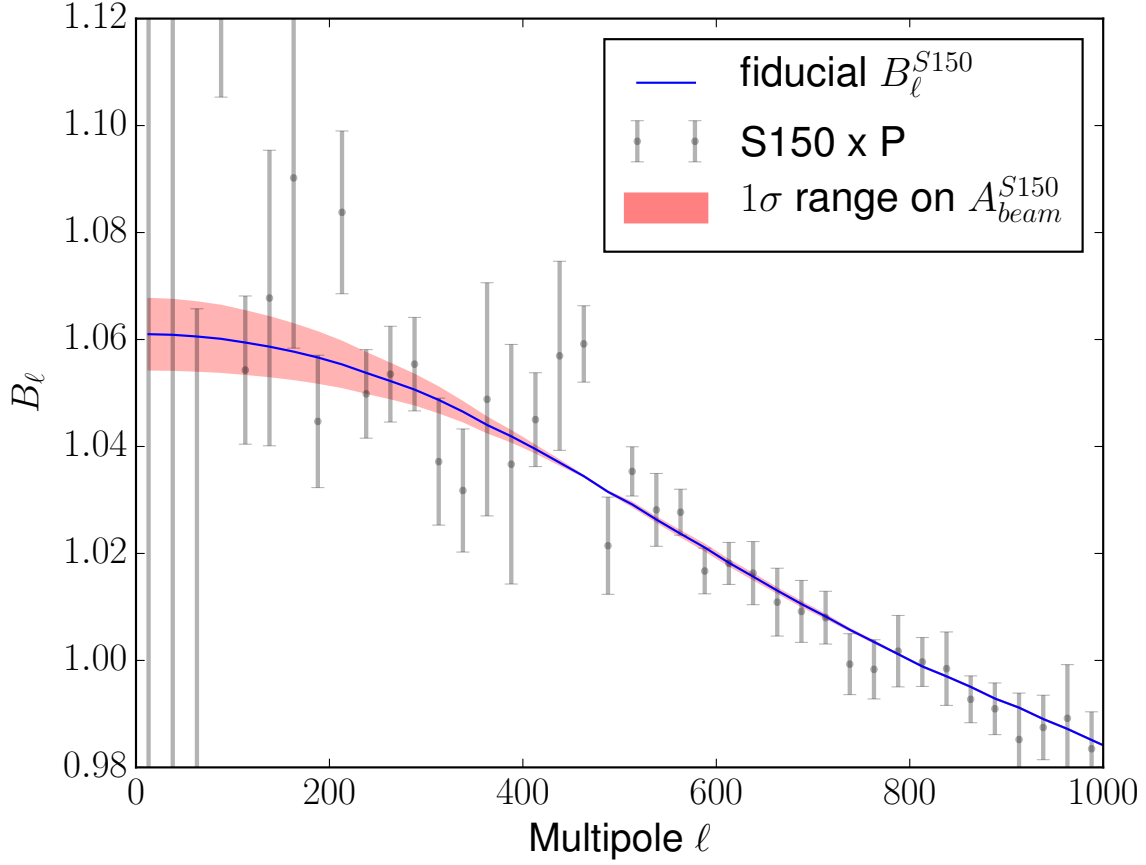
Figure 4.1: The fiducial SPTpol 150 GHz beam (blue), and on top of it, the range of ΔB_ℓ^{S150} that corresponds to 1-σ uncertainties in the A_{beam}^{S150} parameter (red region). Gray data points with error bars represent the right hand side of Equation 4.5.

Plug it into Eq. 4.1,

$$C_\beta^{th} = K_{\beta\beta'}^{-1} P_{\beta'\lambda} K_{\lambda\lambda'} P_{\lambda'l} C_l^{th}$$

From Eq. 4.4,

$$\text{final } D_b^{th} = P_{b\beta} S_{\beta\beta} C_\beta^{th} = \left(P_{b\beta} S_{\beta\beta} K_{\beta\beta'}^{-1} P_{\beta'\lambda} K_{\lambda\lambda'} P_{\lambda'l} \right) C_l^{th}$$

The quantity in parentheses above is our bandpower window function. $K_{\lambda\lambda'}$ and $K_{\beta\beta'}$

are defined in Eq. 4.2 and Eq. 4.3.

4.6   T-to-P Leakage

Through various systematic effects, it is possible for the temperature measurements to leak into polarization measurements. We correct for the "monopole" leakage and the "leakage beam" in the same way as H18. To summarize, we subtract a scaled copy of the T map from the Q and U maps: $Q \to Q - \epsilon^Q T$ and $U \to U - \epsilon^U T$, where the coefficients ϵ^Q and ϵ^U are estimated from the ratio of half-dataset cross-correlated maps. We estimate ϵ^Q to be $0.020(0.032)$ for $150(95)$ GHz, and ϵ^U to be $0.007(-0.022)$ for $150(95)$ GHz. The leakage beam for 95 GHz is negligible, and the leakage beam for 150 GHz can be well explained by differential beam ellipticity: $G_\ell^{TE} = 7.38 \times 10^{-10} \cdot \ell^2$ and $G_\ell^{EE} = 6.40 \times 10^{-19} \cdot \ell^4$. We subtract $G_\ell^{TE} C_\ell^{TT}$ from the $C_\ell^{95T \times 150E}$ and $C_\ell^{150T \times 150E}$ bandpowers, and we subtract $G_\ell^{EE} C_\ell^{TT}$ from the $C_\ell^{150E \times 150E}$ bandpowers.

As in Dutcher et al. [2021], the common-mode filter introduces a bias in the TE spectra, also the TE transfer function is not designed to perfectly recover the simulated TE spectra. We define this "TE bias" as the difference between unbiased simulated bandpowers and theory bandpowers with window function:

$$
\begin{aligned}
TE\mathrm{bias}^{i \times j} &= C_{\beta,sim}^{i \times j} - C_{\beta,th}^{i \times j} \\
&= K_{\beta\beta'}^{-1} P_{\beta'\lambda} \widetilde{C}_{\lambda,sim}^{i \times j} - K_{\beta\beta'}^{-1} P_{\beta'\lambda} K_{\lambda\lambda'} P_{\lambda'l} C_{l,th}^{i \times j} \\
&= K_{\beta\beta'}^{-1} P_{\beta'\lambda} (\widetilde{C}_{\lambda,sim}^{i \times j} - K_{\lambda\lambda'} P_{\lambda'l} C_{l,th}^{i \times j})
\end{aligned}
$$

where $i, j \in \{95GHz, 150GHz\}$ and $i \times j$ denotes the cross-spectrum between the T map of i band and the E map of j band. We apply this correction on our SPTpol bandpowers as $C_\beta^{i \times j} \to C_\beta^{i \times j} - TE\mathrm{bias}^{i \times j}$.

CHAPTER 5

BANDPOWERS

Following the procedures in the previous chapter, we unbias the low-ℓ focused power spectra and the high-ℓ focused power spectra separately, using the appropriate version of filter transfer function F in each case. The final bandpowers are stitched together from $50 < \ell < 500$ of the low-ℓ focused power spectra and $500 < \ell < 8000$ of the high-ℓ focused power spectra. The reason for stitching at $\ell = 500$ is explained in Appendix B.

We report our final unbiased bandpowers in Figures 5.1 and 5.2, and Tables 5.1 and 5.2. The error bars are the square root of the diagonal elements of the bandpower covariance matrix without "further conditioning" (see Section 5.3), and they include contributions from sample variance and noise. We also show our minimum-variance bandpowers alongside other contemporary measurements of the CMB in Figures 5.3 and 5.4.

Table 5.1: SPTpol TE bandpowers from the full 500 deg^2 dataset. The bandpowers D_b and uncertainties σ in each ℓ bin are given in units of μK^2. The uncertainties are the square root of the diagonal elements of the bandpower covariance matrix, and they do not include beam or calibration uncertainties.

ℓ Range	95×95 GHz		$95T \times 150E$		$150T \times 95E$		150×150 GHz	
	D_b	σ	D_b	σ	D_b	σ	D_b	σ
$50 - 100$	-7.5	9.8	-6.2	5.2	-5.2	9.9	-7.0	5.3
$100 - 150$	-65.6	10.7	-56.5	8.4	-65.2	10.8	-57.2	8.5
$150 - 200$	-24.9	9.0	-36.4	7.0	-25.4	9.2	-36.1	7.1
$200 - 250$	13.3	7.7	23.0	6.0	14.3	7.8	23.8	6.1
$250 - 300$	84.4	11.6	89.5	11.1	84.8	11.7	90.9	11.3
$300 - 350$	136.2	14.3	143.3	14.0	134.8	14.4	141.1	14.2
$350 - 400$	36.0	11.8	35.3	11.5	36.3	11.9	34.9	11.7
$400 - 450$	-30.6	10.5	-32.3	10.3	-30.8	10.6	-32.2	10.3

Table 5.1 continued from previous page

ℓ Range	95×95 GHz		$95T \times 150E$		$150T \times 95E$		150×150 GHz	
	D_b	σ	D_b	σ	D_b	σ	D_b	σ
$450 - 500$	-65.8	9.3	-62.1	9.0	-64.9	9.4	-60.8	9.1
$500 - 550$	-19.1	9.9	-22.5	9.3	-19.5	9.9	-22.9	9.3
$550 - 600$	16.2	11.1	7.5	10.6	16.7	11.1	7.5	10.6
$600 - 650$	21.0	13.0	17.4	12.7	22.1	13.1	18.0	12.7
$650 - 700$	-48.0	13.3	-50.4	13.0	-47.6	13.3	-50.4	13.0
$700 - 750$	-115.3	13.8	-113.1	13.5	-115.2	13.8	-112.7	13.4
$750 - 800$	-119.1	12.4	-115.3	11.9	-116.8	12.4	-113.4	11.9
$800 - 850$	-38.7	8.8	-38.4	8.2	-39.4	8.8	-38.9	8.1
$850 - 900$	35.6	9.2	33.5	8.6	35.7	9.1	33.3	8.6
$900 - 950$	44.8	8.7	47.9	8.3	43.9	8.7	47.3	8.3
$950 - 1000$	13.8	9.2	11.8	8.8	12.3	9.1	10.8	8.8
$1000 - 1050$	-63.0	7.9	-64.8	7.6	-60.6	7.8	-63.0	7.5
$1050 - 1100$	-68.5	6.9	-70.7	6.6	-67.9	6.9	-69.3	6.6
$1100 - 1150$	-42.1	6.2	-45.3	5.6	-41.7	6.2	-45.2	5.6
$1150 - 1200$	-11.9	5.5	-14.3	4.8	-11.8	5.4	-14.0	4.8
$1200 - 1250$	15.7	4.9	16.1	4.5	14.8	4.9	15.4	4.4
$1250 - 1300$	-16.8	5.3	-19.4	4.9	-16.6	5.3	-19.2	4.9
$1300 - 1350$	-41.4	5.6	-47.2	5.2	-41.7	5.6	-47.6	5.2
$1350 - 1400$	-58.4	5.5	-55.4	5.0	-57.9	5.4	-54.7	4.9
$1400 - 1450$	-37.1	4.5	-40.8	3.9	-36.7	4.5	-40.7	3.8
$1450 - 1500$	-8.2	4.1	-10.5	3.4	-8.7	4.1	-10.2	3.3
$1500 - 1550$	6.3	3.8	4.9	3.1	6.6	3.7	5.0	3.1

Table 5.1 continued from previous page

ℓ Range	95×95 GHz		$95T \times 150E$		$150T \times 95E$		150×150 GHz	
	D_b	σ	D_b	σ	D_b	σ	D_b	σ
$1550 - 1600$	-2.2	3.7	0.4	3.2	-1.5	3.6	0.9	3.1
$1600 - 1650$	-13.6	3.4	-12.8	2.9	-13.3	3.3	-12.7	2.8
$1650 - 1700$	-25.6	2.9	-29.3	2.4	-25.6	2.9	-29.4	2.4
$1700 - 1750$	-24.9	2.6	-24.8	2.1	-23.4	2.6	-23.6	2.0
$1750 - 1800$	-12.7	2.6	-14.0	1.8	-12.8	2.5	-13.5	1.8
$1800 - 1850$	-6.1	2.3	-7.5	1.7	-7.0	2.3	-8.2	1.6
$1850 - 1900$	0.0	2.5	-3.3	1.8	0.0	2.4	-3.4	1.7
$1900 - 1950$	-9.9	2.3	-12.2	1.7	-10.2	2.2	-12.7	1.6
$1950 - 2000$	-20.0	2.2	-19.8	1.6	-19.6	2.1	-20.0	1.5
$2000 - 2100$	-12.9	1.5	-14.0	1.0	-13.1	1.4	-14.2	0.9
$2100 - 2200$	-1.7	1.2	-3.1	0.8	-2.0	1.2	-3.3	0.7
$2200 - 2300$	-5.8	1.2	-5.5	0.8	-5.6	1.1	-5.0	0.7
$2300 - 2400$	-6.5	1.1	-8.5	0.7	-6.4	1.0	-8.3	0.6
$2400 - 2500$	-4.7	1.1	-2.3	0.6	-4.8	1.0	-2.3	0.5
$2500 - 2600$	-1.8	1.0	-3.0	0.5	-1.5	0.9	-2.9	0.5
$2600 - 2700$	-3.5	1.1	-4.3	0.5	-3.9	0.9	-4.2	0.4
$2700 - 2800$	-3.1	1.0	-2.3	0.5	-3.1	0.8	-2.1	0.4
$2800 - 2900$	-2.3	1.1	-1.7	0.5	-2.0	0.8	-1.3	0.4
$2900 - 3000$	-1.4	1.1	-1.9	0.5	-2.4	0.8	-2.2	0.4
$3000 - 3500$	-1.0	0.5	-0.6	0.2	-0.8	0.3	-0.5	0.2
$3500 - 4000$	0.0	0.7	-0.2	0.3	-0.5	0.4	-0.5	0.2
$4000 - 4500$	-0.9	0.9	0.1	0.4	-1.0	0.5	0.1	0.2

Table 5.1 continued from previous page

ℓ Range	95 × 95 GHz		95T × 150E		150T × 95E		150 × 150 GHz	
	D_b	σ	D_b	σ	D_b	σ	D_b	σ
$4500 - 5000$	-0.6	1.3	0.4	0.5	-1.1	0.7	0.0	0.3
$5000 - 6000$	-1.3	1.6	1.0	0.6	0.7	0.7	0.1	0.3
$6000 - 7000$	-2.3	3.4	0.9	1.0	-1.3	1.3	0.0	0.4
$7000 - 8000$	35.3	8.3	4.2	2.1	4.1	2.6	0.4	0.6

Table 5.2: SPTpol EE bandpowers from the full 500 deg^2 dataset. The bandpowers D_b and uncertainties σ in each ℓ bin are given in units of μK^2. The uncertainties are the square root of the diagonal elements of the bandpower covariance matrix, and they do not include beam or calibration uncertainties.

ℓ Range	95 × 95 GHz		95 × 150 GHz		150 × 150 GHz	
	D_b	σ	D_b	σ	D_b	σ
$50 - 100$	0.7	0.5	0.6	0.2	0.4	0.1
$100 - 150$	1.2	0.4	1.2	0.2	1.2	0.2
$150 - 200$	0.6	0.3	0.6	0.2	0.7	0.1
$200 - 250$	0.5	0.2	0.8	0.2	0.8	0.1
$250 - 300$	4.4	0.6	4.4	0.5	4.6	0.5
$300 - 350$	14.1	1.3	14.5	1.2	14.9	1.2
$350 - 400$	19.9	1.6	20.4	1.6	20.8	1.6
$400 - 450$	16.7	1.4	16.8	1.4	16.9	1.4
$450 - 500$	11.5	1.0	11.2	0.9	11.0	0.9
$500 - 550$	7.6	0.8	7.6	0.7	7.6	0.7
$550 - 600$	11.7	1.2	11.5	1.1	11.8	1.1
$600 - 650$	31.1	2.3	31.0	2.2	31.0	2.2

Table 5.2 continued from previous page

ℓ Range	95 × 95 GHz		95 × 150 GHz		150 × 150 GHz	
	D_b	σ	D_b	σ	D_b	σ
$650 - 700$	38.1	2.6	38.6	2.5	39.4	2.5
$700 - 750$	31.8	2.1	31.9	2.0	31.8	2.0
$750 - 800$	19.1	1.6	19.3	1.5	19.4	1.5
$800 - 850$	12.0	1.0	12.1	0.9	11.9	0.9
$850 - 900$	16.8	1.2	17.5	1.0	18.1	1.0
$900 - 950$	27.8	1.9	28.1	1.8	28.4	1.8
$950 - 1000$	37.7	2.5	37.6	2.4	37.6	2.3
$1000 - 1050$	36.0	2.1	36.0	1.9	36.4	1.9
$1050 - 1100$	25.4	1.7	25.3	1.5	25.1	1.5
$1100 - 1150$	12.6	1.1	13.0	0.9	13.5	0.9
$1150 - 1200$	11.4	1.1	12.2	0.8	12.7	0.8
$1200 - 1250$	20.5	1.4	20.1	1.2	20.6	1.2
$1250 - 1300$	27.2	1.7	27.9	1.5	28.2	1.5
$1300 - 1350$	28.9	1.5	29.5	1.3	30.6	1.3
$1350 - 1400$	22.3	1.2	21.8	1.0	21.6	1.0
$1400 - 1450$	12.5	0.9	12.8	0.7	12.9	0.7
$1450 - 1500$	10.6	0.9	10.4	0.6	10.1	0.6
$1500 - 1550$	16.1	1.1	14.9	0.8	14.9	0.8
$1550 - 1600$	16.9	1.2	18.0	0.9	18.2	0.9
$1600 - 1650$	21.4	1.2	21.3	0.9	21.4	0.9
$1650 - 1700$	15.4	1.1	15.5	0.8	15.6	0.8
$1700 - 1750$	10.1	1.0	10.2	0.6	10.5	0.6

Table 5.2 continued from previous page

ℓ Range	95 × 95 GHz		95 × 150 GHz		150 × 150 GHz	
	D_b	σ	D_b	σ	D_b	σ
$1750 - 1800$	6.9	0.9	6.9	0.5	7.3	0.4
$1800 - 1850$	8.4	0.9	8.2	0.5	8.3	0.5
$1850 - 1900$	10.3	0.9	10.1	0.5	9.9	0.5
$1900 - 1950$	9.4	1.0	10.6	0.6	10.9	0.6
$1950 - 2000$	9.8	1.1	10.1	0.6	10.6	0.5
$2000 - 2100$	5.8	0.6	6.1	0.3	6.2	0.3
$2100 - 2200$	5.7	0.7	5.0	0.3	5.0	0.3
$2200 - 2300$	6.8	0.7	5.7	0.3	5.7	0.3
$2300 - 2400$	3.7	0.8	3.9	0.3	4.1	0.2
$2400 - 2500$	2.6	0.7	2.9	0.3	2.4	0.2
$2500 - 2600$	2.3	0.8	3.0	0.3	3.0	0.2
$2600 - 2700$	2.6	0.9	1.9	0.3	2.0	0.2
$2700 - 2800$	3.0	0.9	1.5	0.3	1.5	0.2
$2800 - 2900$	3.2	1.0	1.3	0.3	1.4	0.2
$2900 - 3000$	0.3	1.1	0.8	0.4	0.7	0.3
$3000 - 3500$	0.3	0.6	0.4	0.2	0.5	0.1
$3500 - 4000$	0.6	0.9	-0.1	0.3	0.3	0.2
$4000 - 4500$	0.0	1.3	0.5	0.4	-0.3	0.2
$4500 - 5000$	-1.1	1.9	-0.3	0.5	-0.2	0.3
$5000 - 6000$	-0.3	2.6	-0.5	0.6	-0.4	0.3
$6000 - 7000$	3.9	6.1	-1.0	1.3	0.2	0.6
$7000 - 8000$	-28.8	15.9	-3.2	2.8	0.9	1.0
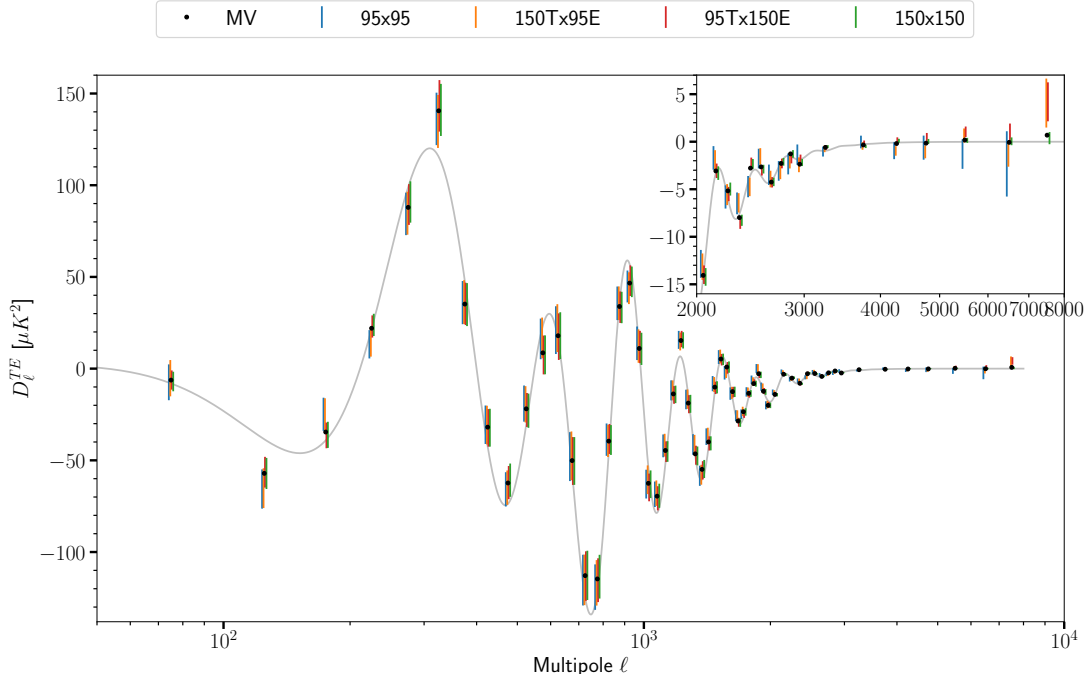
Figure 5.1: SPTpol 500 deg^2 TE angular power spectrum, with an inset plot zooming in at high ℓ. The gray line is the *Planck* best-fit ΛCDM model. Black points are the SPTpol minimum-variance bandpowers (see Section 5.3), and the colored error bars are the square root of the diagonal elements of the bandpower covariance matrix without "further conditioning". Small offsets in ℓ have been added for plotting purposes.

5.1 Jackknife Null Tests

We perform jackknife null tests before the unbiasing step to look for potential systematic contamination. In each test, we sort the 50 map bundles based on that potential systematic, and difference each pair of bundles that are maximally different in that metric. The spectra of these null map bundles are expected to be zero on average, otherwise it indicates our data is contaminated by that systematic.

We perform a total of seven jackknife null tests. The left-right, sun, and moon jackknives are done in the same way as H18. For the azimuth jackknife, in order to maximize sensitivity to azimuth, we no longer use the same 50 map bundles for this test; instead we re-bundle every observation sorted by azimuth into a new set of 50 bundles. We test for potential
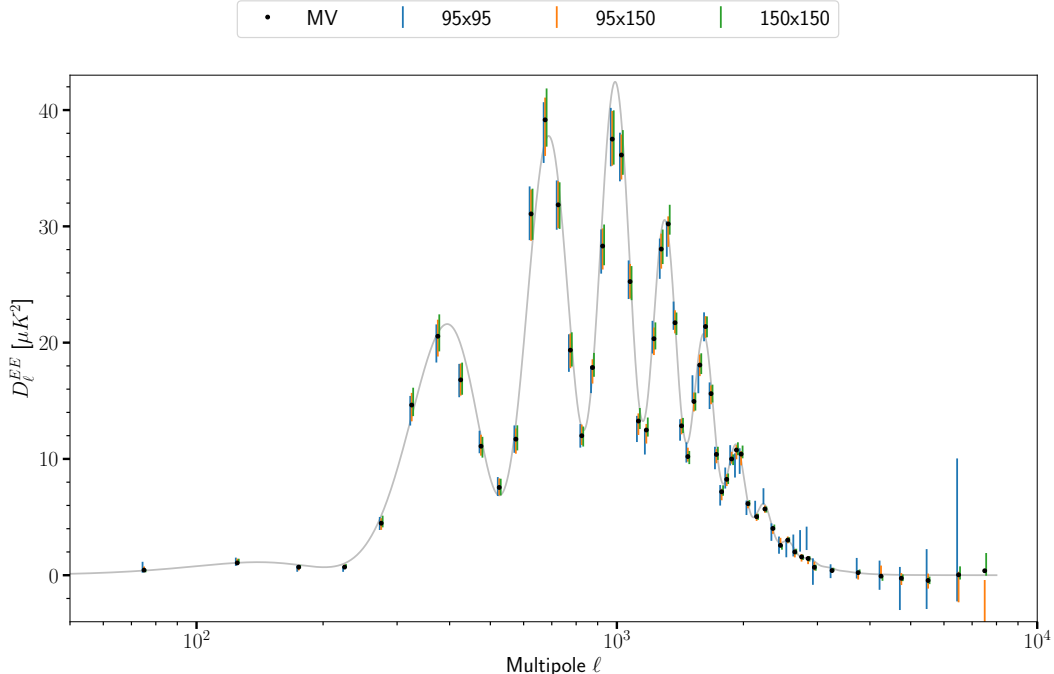
Figure 5.2: SPTpol 500 deg^2 EE angular power spectrum. The gray line is the *Planck* best-fit ΛCDM model. Black points are the SPTpol minimum-variance bandpowers (see Section 5.3), and the colored error bars are the square root of the diagonal elements of the bandpower covariance matrix without "further conditioning". Small offsets in ℓ have been added for plotting purposes.

contamination coming from a building at 153° azimuth by sorting and differencing these new 50 bundles based on distance to 153° azimuth. For the chronological null tests, unlike H18, we perform three separate jackknives: 1st half minus 2nd half within lead-trail observations, 1st half minus 2nd half within full-field observations, and "1st half of lead-trail plus 1st half of full-field" minus "2nd half of lead-trail plus 2nd half of full-field". This way, for all the jackknives above, their null spectra in signal-only simulations are expected to be small, and we verified that they are indeed negligible, therefore we do not subtract the simulated null spectra from the jackknife null spectra as in H18. Instead, we compute the χ^2 of jackknife null spectra with respect to zero.

In the left-right jackknife, we found excess power in the TE spectra. Looking through each null map bundle, we only saw this excess power in a few date ranges in 2013. We removed
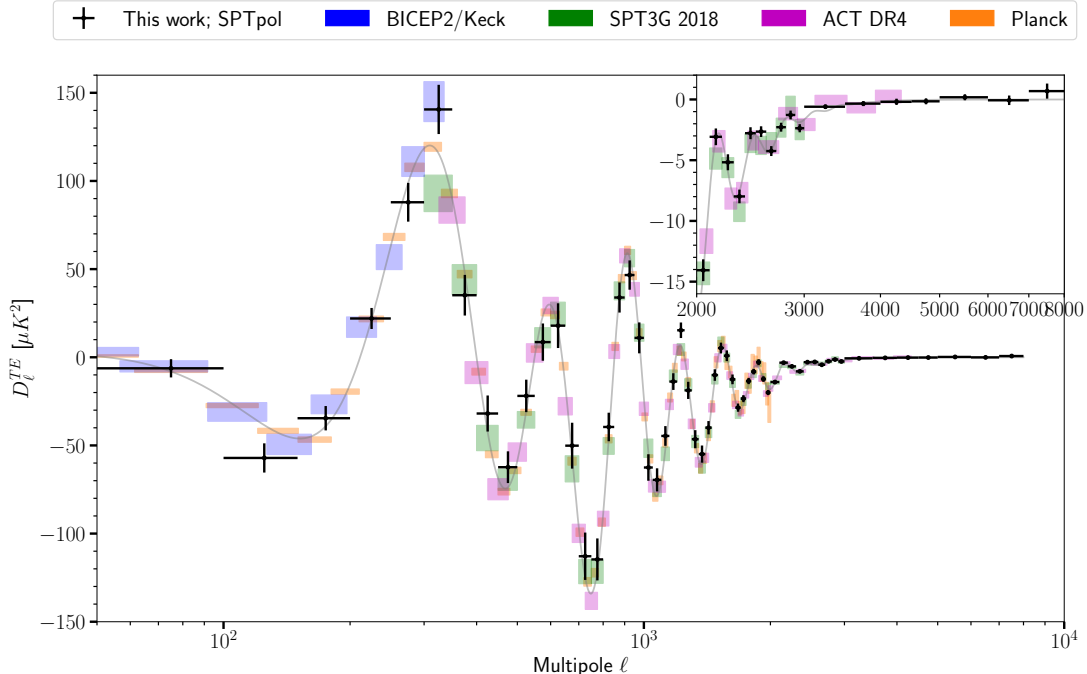
Figure 5.3: SPTpol and other contemporary measurements of the TE angular power spectrum, with an inset plot zooming in at high ℓ. Black points and error bars are the SPTpol minimum-variance bandpowers in this work. SPT-3G 2018 $TT/TE/EE$ bandpowers are in green [Balkenhol et al., 2023], BICEP2/Keck in blue [BICEP2 and Keck Array Collaborations et al., 2015], ACT DR4 in magenta [Choi et al., 2020], and *Planck* in orange. The gray line is the *Planck* best-fit ΛCDM model.

observations between 2013 July 27 to August 9, October 25 to November 1, and November 15 to November 27. A total of 228 observations were removed. In the azimuth jackknife, we also found excess power in the lowest ℓ-bin ($50 < \ell < 100$) of the 150 GHz spectra. It was a coherent azimuth-dependent systematic contamination, and it was concentrated in a small area in 2D Fourier space. As a solution, we applied a uv-mask in that area to mask it out, for the low-ℓ focused dataset only, for both the data maps and simulated maps so that it is reflected in the transfer function.

After these fixes, we present the probabilities to exceed (PTEs) for these jackknife χ^2 tests in Table 5.3. None of these PTEs are anomalously close to zero or one. We conclude that our data does not contain statistically significant systematic biases from the sources
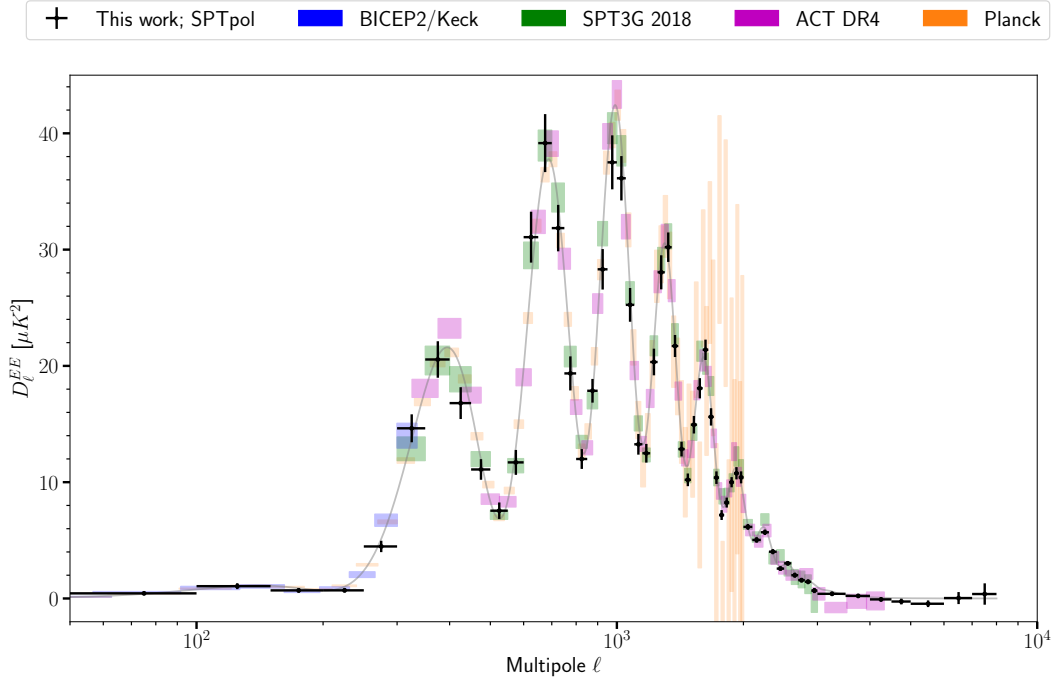
Figure 5.4: SPTpol and other contemporary measurements of the EE angular power spectrum. Black points and error bars are the SPTpol minimum-variance bandpowers in this work. SPT-3G 2018 $TT/TE/EE$ bandpowers are in green [Balkenhol et al., 2023], BICEP2/Keck in blue [BICEP2 and Keck Array Collaborations et al., 2015], ACT DR4 in magenta [Choi et al., 2020], and *Planck* in orange. The gray line is the *Planck* best-fit ΛCDM model.

tested here.

Table 5.3: PTE values of each jackknife null test in this work.

	150 GHz		95 GHz	
	EE	TE	EE	TE
Lead-Trail 1st-2nd	0.81	0.24	0.70	0.39
Full-Field 1st-2nd	0.29	0.31	0.15	0.35
both 1st - both 2nd	0.13	0.10	0.36	0.04
left-right	0.05	0.20	0.28	0.18
sun	0.17	0.27	0.69	0.70
moon	0.59	0.81	0.02	0.33
azimuth	0.43	0.40	0.23	0.38

5.2 Bandpower Covariance Matrix

Measuring the bandpowers is just half the story; we also need to know their uncertainties and the correlation of these uncertainties, i.e., the bandpower covariance matrix. It accounts for contributions from both sample variance and noise variance. From our 95 and 150 GHz data, and temperature and E-mode maps, there are seven possible TE or EE bandpowers one can cross-correlate ($95T \times 95E$, $95T \times 150E$, $150T \times 95E$, $150T \times 150E$, $95E \times 95E$, $95E \times 150E$, $150E \times 150E$); we concatenate these seven bandpowers, and therefore our covariance matrix has a 7×7 block structure.

H18 added noise map realizations to noiseless simulated maps and then calculated the bandpower covariance matrix from them, but in this work we did not make noisy sim maps. We found the (co)variance of the noise realizations to be numerically noisy at high ℓ (especially for 95 GHz), so instead, we use the expected variance in the algebraic form for the noise part. To be more specific, the diagonal elements of each block in the covariance matrix are expected to be: [Lueker et al., 2010]

$$\Xi_{bb}^{AB,CD} \simeq \frac{1}{\nu_b}(\langle D_b^{AC} \rangle \langle D_b^{BD} \rangle + \langle D_b^{AD} \rangle \langle D_b^{BC} \rangle) \tag{5.1}$$

where ν_b is the effective number of degrees of freedom, D_b is the cross-spectrum between two maps, and each map in $\{A, B, C, D\}$ has a signal power (S_b) and a noise power (N_b). If A, B, C, D are all different maps for example, the noise in these maps are expected to be uncorrelated, so only the signal part is expected to remain: $\Xi_{bb} = 2S_b^2/\nu_b$. As another example, if A, B, C, D are all the same map, the noise parts will be completely correlated, so the expected variance becomes $\Xi_{bb} = (2S_b^2 + 4S_b N_b + 2N_b^2)/\nu_b$.

We split the covariance into a sum of two parts and obtain them differently, the signal-only part (S^2) and the noisy part ($S \times N$ and N^2). The S^2 part is not very noisy numerically, so we calculate it directly from the auto-spectra of 226 noiseless simulated maps, as in Crites

et al. [2015]. In addition, we use Eq. 5.1 backwards to obtain ν_b for use in the next part:

- Let A = C = 95 GHz T map, B = D = 95 GHz E map, compute ν_b as ν_b^{TE95};

- Let A = C = 150 GHz T map, B = D = 150 GHz E map, compute ν_b as ν_b^{TE150};

- Let A = C = 95 GHz E map, B = D = 95 GHz E map, compute ν_b as ν_b^{EE95};

- Let A = C = 150 GHz E map, B = D = 150 GHz E map, compute ν_b as ν_b^{EE150};

Finally, our estimate of ν_b^{TE} is the average of ν_b^{TE95} and ν_b^{TE150}, and our estimate of ν_b^{EE} is the average of ν_b^{EE95} and ν_b^{EE150}. For the $S \times N$ and N^2 part, we again use Eq. 5.1 to obtain $\Xi_{bb}^{AB,CD}$ using the average spectra S_b of noiseless simulations, the average spectra N_b of noise realizations, and the aforementioned ν_b^{TE} and ν_b^{EE}.

The off-diagonal elements of each block in the covariance matrix are expected to reflect mode-coupling from two sources, apodization mask and lensing. These elements are again numerically noisy, so we model them in the following way.

Lensing introduces mode-coupling in a "checkerboard" pattern [Benoit-Lévy et al., 2012], and it is furthermore amplified and distorted under the flat-sky approximation we use. To estimate this resulting correlation matrix, we take 3,000 pairs of noiseless simulated HEALPix[1] skies, (one lensed and one unlensed,) and convert them into flat-sky maps under the oblique Lambert azimuthal equal-area projection. We apply the same apodization mask as used for the data and compute their TE and EE auto-spectra. The correlation matrix estimated using the 3,000 unlensed spectra only contains mode-coupling from the mask, and we model it in a similar way as H18, averaging elements the same distance from the diagonal, and setting all elements greater than $\Delta \ell = 50$ from the diagonal to zero. On the other hand, the correlation matrix estimated using the 3,000 lensed spectra contains mode-coupling from both the mask and lensing, therefore we subtract from it the aforementioned correlation matrix

---

1. Górski et al. [2005]

of unlensed spectra, and we take the remainder as our model of the lensing "checkerboard". We compute these model correlation matrices separately for $TE \times TE$ and $EE \times EE$.

We arrange these $TE \times TE$ or $EE \times EE$ model correlation matrices into the same 7×7 block structure; for a $TE \times EE$ off-diagonal block, we take the arithmetic mean of $TE \times TE$ and $EE \times EE$. These correlation matrices are then converted into covariance using the main diagonal of the 7×7 bandpower covariance matrix, but for the lensing "checkerboard" part, only the S^2 part of the main diagonal is used, since noise is expected to have zero contribution. Finally, all the off-diagonal elements from the lensing part and the masking part are added to the bandpower covariance matrix. This matrix is then binned to the same coarse ℓ bins as our bandpowers.

The 7×7 bandpower covariance matrix constructed this way is positive definite. It has 392×392 elements, but we note that only 226 independent simulated auto-spectra were used in its construction, leading to numerical instability (near rank deficiency) as we will see in the internal consistency tests (Section 5.3).

Our beam uncertainty comes from 3 sources, and as in H18, we do not incorporate them into the bandpower covariance matrix when performing cosmology fits. Instead, we compute beam uncertainty eigenmodes from each of them, and treat their amplitudes as nuisance parameters during cosmology fits. When performing internal consistency tests however, we indeed add the appropriate contribution from beams into the covariance matrix.

The 1st source of beam uncertainty is the variation between the 5 Venus observations. From each Venus observation, we make an instance of B_ℓ^2, and we make them in the same way for the 95 and 150 GHz bands. To capture the correlation between bands, we concatenate the three types of spectra ($95 \times 95, 95 \times 150, 150 \times 150$), and compute its 3×3-block covariance matrix. This is the covariance matrix of B_ℓ^2, we extract 4 eigenmodes from this matrix, and then under the first-order approximation, we convert it into a bandpower covariance matrix $D_\ell \, \mathrm{cov}(B_\ell^2)/B_\ell^2$ where D_ℓ is CMB bandpowers from a fiducial model. The 2nd source is the

28

uncertainty of pointing jitter sizes. The nominal pointing jitter size is estimated by fitting 2D Gaussians to the two brightest point sources in our field, and then averaged over the two. Now for the pointing jitter size of each source individually, we make the average Venus B_ℓ^2 in the same 3-block structure, and similarly we extract 1 eigenmode from its covariance matrix.

The 3rd source of beam uncertainty comes from the low-ℓ beam shape, described by $A_{\mathrm{beam}}^{\mathrm{S95}}$ and $A_{\mathrm{beam}}^{\mathrm{S150}}$ in Section 4.4. By definition the beam uncertainty $\delta B_\ell = \delta A_{\mathrm{beam}} \cdot \Delta B_\ell$ where δA_{beam} is the 1-σ uncertainty of the A_{beam} parameter. From this we can construct bandpower correlation matrices by generalizing the method in Aylor et al. [2017]. With i, j, k, l denoting either SPTpol 95 GHz or 150 GHz,

$$\rho_{\ell\ell'}^{i\times j, k\times l} = \left\langle \frac{\delta D_\ell^{i\times j}}{D_\ell} \cdot \frac{\delta D_{\ell'}^{k\times l}}{D_{\ell'}} \right\rangle$$

$$\text{where} \quad \frac{\delta D_\ell^{i\times j}}{D_\ell} = (1 + \frac{\delta B_\ell^i}{B_\ell})^{-1}(1 + \frac{\delta B_\ell^j}{B_\ell})^{-1} - 1$$

$$\text{to first order,} \quad = -\frac{\delta B_\ell^i}{B_\ell} - \frac{\delta B_\ell^j}{B_\ell}$$

$$\Rightarrow \rho_{\ell\ell'}^{i\times j, k\times l} = \left\langle \frac{\delta B_\ell^i}{B_\ell} \frac{\delta B_{\ell'}^k}{B_{\ell'}} \right\rangle + \left\langle \frac{\delta B_\ell^i}{B_\ell} \frac{\delta B_{\ell'}^l}{B_{\ell'}} \right\rangle + \left\langle \frac{\delta B_\ell^j}{B_\ell} \frac{\delta B_{\ell'}^k}{B_{\ell'}} \right\rangle + \left\langle \frac{\delta B_\ell^j}{B_\ell} \frac{\delta B_{\ell'}^l}{B_{\ell'}} \right\rangle$$

$$= \frac{\delta B_\ell^i}{B_\ell} \frac{\delta B_{\ell'}^k}{B_{\ell'}} \mathrm{corr}(A_{\mathrm{beam}}^i, A_{\mathrm{beam}}^k) + \frac{\delta B_\ell^i}{B_\ell} \frac{\delta B_{\ell'}^l}{B_{\ell'}} \mathrm{corr}(A_{\mathrm{beam}}^i, A_{\mathrm{beam}}^l)$$

$$+ \frac{\delta B_\ell^j}{B_\ell} \frac{\delta B_{\ell'}^k}{B_{\ell'}} \mathrm{corr}(A_{\mathrm{beam}}^j, A_{\mathrm{beam}}^k) + \frac{\delta B_\ell^j}{B_\ell} \frac{\delta B_{\ell'}^l}{B_{\ell'}} \mathrm{corr}(A_{\mathrm{beam}}^j, A_{\mathrm{beam}}^l)$$

where $\mathrm{corr}(A_{\mathrm{beam}}^{\mathrm{S95}}, A_{\mathrm{beam}}^{\mathrm{S150}})$ was found to be 0.45 during the fits in Section 4.4 if $A_{\mathrm{beam}}^{\mathrm{S95}}$ and $A_{\mathrm{beam}}^{\mathrm{S150}}$ were allowed to float simultaneously. We stack these correlation matrices into a 3×3 block structure in the order of $(95\times95, 95\times150, 150\times150)$, and we extract 2 eigenmodes from this matrix. Finally, we use model bandpowers D_ℓ to convert it into a bandpower covariance matrix $\rho_{\ell\ell'}^{i\times j, k\times l} D_\ell^{i\times j} D_{\ell'}^{k\times l}$ [Dutcher et al., 2021]. These 4+1+2 beam uncertainty eigenmodes are treated as nuisance parameters in Section 6.2, with their eigenvalues being the 1-σ widths

of the Gaussian priors.

5.3   Internal Consistency

We expect the multifrequency bandpowers to be consistent with each other. With this expectation, we can construct minimum-variance TE and EE bandpowers in the same way as Dutcher et al. [2021], and perform the same chi-squared test to test this expectation. The result is that χ^2 is too high for 280 degrees of freedom (392 multifrequency bandpowers $-$ 112 minimum-variance bandpowers).

We suspect the bandpower covariance matrix to be numerically unstable during inversion, which means further conditioning is needed. If the matrix is nearly rank deficient, a spurious eigenmode would have a small numerical value as its eigenvalue. Therefore, we choose some cutoff threshold, and set all eigenvalues below it to very large values, essentially erasing any information along that eigenmode from our covariance matrix. If that eigenmode is indeed spurious, the cosmological parameter constraints should not widen too much after erasing information along this eigenmode, so we will test this criterion in the pipeline consistency tests (Section 6.3).

One last test when choosing this cutoff threshold, is to use this conditioned covariance matrix to compute the χ^2 of the 226 simulated auto-spectra. If N eigenmodes are erased, the distribution of these 226 χ^2 should be consistent with a χ^2 pdf of $392 - 1 - N$ degrees of freedom, and we quantify this using a Kolmogorov-Smirnov test. After trying various cutoff thresholds, we find that a threshold of "2.619×10^{-5} times the largest eigenvalue" passes all the criteria above. There are 57 eigenvalues smaller than this threshold, and they are set to very large values instead. After this further conditioning, the χ^2 in the minimum-variance test becomes $\chi^2 = 257.79$ for 223 degrees of freedom (PTE of 0.0548), and the Kolmogorov-Smirnov test gives a PTE of 0.239. We use this conditioned 7×7 bandpower covariance matrix when fitting cosmology with our full data vector in Chapter 7. However,

the original covariance matrix (before this conditioning) is also saved for later use, as are the 57 eigenvectors that were erased. We will discuss them in Section 7.1.

CHAPTER 6

LIKELIHOOD

We write our likelihood code in the `Cobaya` framework [Torrado and Lewis, 2021], and we use the Markov Chain Monte Carlo sampler [Lewis and Bridle, 2002] to map out the parameter space. For the CMB theory power spectra, we use the emulator published by Bolliet et al. [2023] that provides orders-of-magnitude speed-up over Boltzmann codes, and it was trained in the COSMOPOWER framework [Spurio Mancini et al., 2022] using `CLASS` power spectra [Lesgourgues, 2011, Blas et al., 2011].

6.1   LCDM Parameters

The six ΛCDM parameters in this emulator are: the reionization optical depth τ, $\ln(10^{10}A_s)$ where A_s is the amplitude of primordial scalar perturbations, the scalar spectral index n_s, the baryon density $\Omega_b h^2$, the dark matter density $\Omega_{\rm cdm} h^2$, and the Hubble constant H_0. The emulator also returns the angular size of the sound horizon at recombination $(100\theta_s)$ as a derived parameter, but we note that θ_s in `CLASS` is defined differently than the $\theta_{\rm MC}$ defined in COSMOMC, therefore we never directly compare the θ_s in this work with $\theta_{\rm MC}$ in other works.

SPTpol data alone does not have a strong constraining power on the reionization optical depth τ. As in Balkenhol et al. [2023], we use a *Planck*-based Gaussian prior of $\tau = 0.0540 \pm 0.0074$. We do not apply any prior to the other five ΛCDM parameters.

6.2   Nuisance Parameters

We fit for the temperature and polarization calibration factors in Section 4.4, and we obtained their best-fit values and 1-σ uncertainties. Although we already used these best-fit values to calibrate our data bandpowers, here we still allow the calibration factors to float as nuisance

parameters, with a Gaussian prior centered at unity and 1-σ uncertainties taken from the above. The four nuisance parameters introduced here are $T_{\text{cal}}^{150}, T_{\text{cal}}^{95\text{to}150}, P_{\text{cal}}^{95}$, and P_{cal}^{150}, where $T_{\text{cal}}^{95\text{to}150}$ is the calibration factor of our 95 GHz data w.r.t. our 150 GHz data. This quantity is independent from T_{cal}^{150}, which is calibrated against *Planck*. The Gaussian prior 1-σ on $T_{\text{cal}}^{95\text{to}150}$ is 0.00115. For T_{cal}^{150}, we also need to incorporate the calibration uncertainty of *Planck*, and the resulting Gaussian prior 1-σ is 0.00271. For the polarization calibration factors, their Gaussian prior 1-σ are taken from the findings of H18 (0.01).

We extract a total of 7 beam uncertainty eigenmodes when making the bandpower co-variance matrix, as mentioned in Section 5.2. In our cosmology fits, we allow the bandpowers to have variations along those 7 eigenmodes H_ℓ^n,

$$C_{\ell,n}^{\text{beam}} = A_{\text{beam}}^n H_\ell^n$$

$$C_\ell \rightarrow C_\ell \prod_{n=1}^{7} 1 + C_{\ell,n}^{\text{beam}}$$

where n indexes the eigenmodes, C_ℓ is the theory power spectrum, and A_{beam}^n are the nuisance parameters introduced here as the amplitudes of the eigenmodes. We apply Gaussian priors centered at zero to A_{beam}^n, and the eigenvalues found when we extracted those eigenmodes are used here as the 1-σ widths of the priors.

We introduce a total of 8 nuisance parameters for foreground parameterization, and they are defined in a similar way to H18. For the power spectrum of Galactic dust, we follow the model of Planck Collaboration et al. [2016],

$$D_{\ell,\text{dust}}^{XY95} = A_{80}^{XY95}(\frac{\ell}{80})^{\alpha_{XY}+2}$$

$$D_{\ell,\text{dust}}^{XY150} = A_{80}^{XY150}(\frac{\ell}{80})^{\alpha_{XY}+2}$$

where $XY \in \{TE, EE\}$, the superscripts 95 or 150 denote either frequency band, A_{80} is the

amplitude of the spectrum at $\ell = 80$ in units of μK^2, and α_{XY} is the spectral index. For the cross-frequency power spectra 95×150, we assume dust is 100% correlated, i.e.

$$D_{\ell,\text{dust}}^{XY95 \times 150} = \sqrt{A_{80}^{XY95} \cdot A_{80}^{XY150}} \left(\frac{\ell}{80}\right)^{\alpha_{XY}+2}$$

For all the A_{80} parameters, we use a uniform prior between 0 and 2 μK^2. For α_{XY}, we use a Gaussian prior centered at -2.42 with a σ of 0.02. For polarized extragalactic point sources, we use a single component $D_\ell^{EE} \propto \ell^2$ to model the residual power after masking all sources above 50 mJy in unpolarized flux at 95 or 150 GHz. We introduce the nuisance parameters $D_{3000}^{PSEE,95}$ and $D_{3000}^{PSEE,150}$ as the amplitude of this component at $\ell = 3000$ for the 95 and 150 GHz EE spectra, respectively. The amplitude of this component for the 95×150 EE spectrum is assumed to be $\sqrt{D_{3000}^{PSEE,95} \cdot D_{3000}^{PSEE,150}}$. We apply a uniform prior between 0 and 2 μK^2 on these two parameters.

As in H18, we use one parameter to account for "super-sample lensing" at every step in the Markov chain: [Manzotti et al., 2014]

$$\hat{C}_\ell^{XY}(\mathbf{p}; \kappa) = C_\ell^{XY}(\mathbf{p}) - \frac{\partial \ell^2 C_\ell^{XY}(\mathbf{p})}{\partial \ln \ell} \frac{\kappa}{\ell^2}$$

where $\mathbf{p}$ is the parameter vector, and the nuisance parameter κ is the mean lensing convergence in the field. We apply a Gaussian prior centered at zero with a σ of 0.001 to κ. For aberration, we apply the usual zero-parameter correction to the theory spectra: [Jeong et al., 2014]

$$C_\ell \to C_\ell - C_\ell \frac{d \ln C_\ell}{d \ln \ell} \beta \langle \cos \theta \rangle$$

where $\beta = 0.0012309$ and $\langle \cos \theta \rangle = -0.40$.

6.3   Pipeline Consistency Test

We perform a few consistency tests on our likelihood and fitting pipeline. First, we try to recover the ΛCDM parameters of the input cosmology chosen for making simulated skies in Section 4.3. We take the average of our 226 noise-free simulated bandpowers, thereby reducing sample variance as much as possible, and fit it with the pipeline described in this chapter. As a result, we find the following shifts in the parameter constraints compared to the best-fit values of *Planck* `base_plikHM_TT_lowTEB_lensing`: $(\Delta\Omega_b h^2 = -0.02\sigma, \Delta\Omega_{\mathrm{cdm}} h^2 = 0.05\sigma, \Delta H_0 = -0.05\sigma, \Delta\tau = 0.02\sigma, \Delta(10^9 A_s e^{-2\tau}) = 0.05\sigma, \Delta n_s = 0.01\sigma)$. All six parameters are in excellent agreement.

Furthermore, when making simulated bandpowers, we also make ones using an "alternate cosmology" as previously mentioned. Our alternate cosmology is the same one as H18 $(\Omega_b h^2 = 0.018, \Omega_{\mathrm{cdm}} h^2 = 0.14, \theta_{\mathrm{MC}} = 1.079, \tau = 0.058, A_s = 2.2 \times 10^{-9}, n_s = 0.92)$, with foreground amplitudes doubled. We take the average of these alternate cosmology simulated bandpowers, unbias them with the same kernel used in Chapter 4, and fit them to ΛCDM theory with the same bandpower covariance matrix obtained in Chapter 5. This allows us to test whether the unbiasing kernel and/or the covariance matrix have a strong dependence on the chosen input cosmology. As a result, we find the following shifts in the parameter constraints: $(\Delta\Omega_b h^2 = 0.18\sigma, \Delta\Omega_{\mathrm{cdm}} h^2 = -0.52\sigma, \Delta\theta_s = -0.57\sigma, \Delta\tau = -0.01\sigma, \Delta A_s = -0.26\sigma, \Delta n_s = 0.11\sigma)$. Although this result shows some half-sigma shifts, we note that the θ_{MC} in this cosmology is drastically different from the current best constraints obtained by *Planck* $(\theta_{\mathrm{MC}} =\sim 1.041)$. The 1-$\sigma$ uncertainty on θ_s in this result is 0.00114, which means θ is $\sim 30\sigma$ away from *Planck*. Therefore this is a very stringent test, and it shows our pipeline is quite robust against variations in the chosen input cosmology.

Finally, we verify that the "further conditioning" of the bandpower covariance matrix done in Section 5.3 did not degrade our cosmological parameter constraints too much. In that step, we erased information along 57 eigenmodes of the covariance matrix, and the

assumption was that most of those eigenmodes were spurious in the first place. As a test, we fit our full data bandpowers to ΛCDM cosmology again in the same way, but this time using the bandpower covariance matrix before the further conditioning step. We compare, not the best-fit parameters, but the 1-σ widths of the parameter constraints before and after further conditioning. The result is that the constraints for $10^9 A_s e^{-2\tau}$ degraded by 6%, n_s degraded by 4%, and other parameters less than 2%. We conclude that this assumption is valid and that "further conditioning" is justified.

CHAPTER 7

COSMOLOGICAL CONSTRAINTS

Column (c) of Table 7.1 shows the cosmological parameter constraints from all 7 sets of multifrequency bandpowers in this SPTpol EE/TE dataset. The χ^2 of the best-fit ΛCDM theory curve to the SPTpol data bandpowers is $\chi^2 = 355.91$ for 324 degrees of freedom (PTE of 0.11).

We find the polarized point source power $D_{3000}^{PSEE,95} < 0.45 \mu K^2$ and $D_{3000}^{PSEE,150} < 0.034 \mu K^2$ at 95% confidence. This upper limit in 150 GHz seems to be three times better than H18, but we caution against taking it at face value; if we did not use the prior to constrain $D_{3000}^{PSEE,150}$ between 0 and 2, the best fit would actually prefer a negative value due to the random noise in our bandpowers. Therefore our upper limit on $D_{3000}^{PSEE,150}$ is artificially too tight.

Table 7.1: ΛCDM parameter constraints and 68% uncertainties from the full SPTpol 500 deg^2 dataset (column (c)) and a few data splits (other columns). The top half shows free ΛCDM parameters (with a Gaussian prior on $\tau = 0.0540 \pm 0.0074$), and the bottom half shows derived parameters. H_0 is expressed in units of km s^{-1} Mpc^{-1}.

	(a) $\ell < 1000$ 95 GHz	(b) $\ell < 1000$ 150 GHz	(c) full dataset	(d) $\ell > 1000$ 150 GHz	(e) $\ell > 1000$ 95 GHz
free					
$100\,\Omega_b h^2$	2.221 ± 0.133	2.270 ± 0.125	2.268 ± 0.041	2.211 ± 0.050	2.338 ± 0.083
$\Omega_c h^2$	0.1326 ± 0.0135	0.1224 ± 0.0102	0.1116 ± 0.0052	0.0999 ± 0.0078	0.1062 ± 0.0122
n_s	0.9045 ± 0.0598	0.9403 ± 0.0466	0.9913 ± 0.0236	1.0575 ± 0.0458	1.0329 ± 0.0665
H_0	62.59 ± 5.44	66.93 ± 4.64	70.37 ± 2.18	74.98 ± 3.73	73.25 ± 5.65
$\ln(10^{10} A_s)$	3.021 ± 0.048	3.018 ± 0.041	2.960 ± 0.030	2.906 ± 0.051	2.908 ± 0.067
derived					
$100\,\theta_s$	1.0405 ± 0.0026	1.0422 ± 0.0023	1.0407 ± 0.0015	1.0415 ± 0.0012	1.0410 ± 0.0017
$10^9 A_s e^{-2\tau}$	1.8416 ± 0.0844	1.8349 ± 0.0697	1.7357 ± 0.0466	1.6425 ± 0.0807	1.6437 ± 0.1077
σ_8	0.8195 ± 0.0441	0.7997 ± 0.0416	0.7562 ± 0.0221	0.7106 ± 0.0363	0.7239 ± 0.0557
S_8	0.5448 ± 0.0550	0.5109 ± 0.0464	0.4615 ± 0.0235	0.4102 ± 0.0363	0.4307 ± 0.0563

7.1 Data Splits

We split the SPTpol EE/TE dataset into several subsets to investigate internal consistency, where we compare the best-fit cosmological parameters between the subset and the full SPTpol dataset. We perform seven data splits: the 95 and 150 GHz auto-frequency spectra, the 95×150 cross-frequency spectra, the TE-only and EE-only spectra, and the $\ell < 1000$ and $\ell > 1000$ bandpowers. We fit each subset to ΛCDM cosmology with the same method described in Chapter 6, where only the relevant nuisance parameters are floated, the rest fixed to the best-fit values from the full SPTpol dataset. In order to keep the fitting methodology comparable between the subset and the full dataset, for the case of each subset, we fit the full dataset again, with these same nuisance parameters fixed or floated.

For each subset, we would like to slice the bandpower covariance matrix to keep only the relevant blocks, however it would be mathematically wrong to slice the matrix after the "further conditioning" described in Section 5.3. We instead slice the original covariance matrix, but in order to keep the methodology "apples-to-apples" between the subset and the full dataset, we need to appropriately account for the 57 erased eigenmodes here. Therefore, as part of the likelihood code, whenever we subtract the theory ΛCDM curve from the SPTpol bandpowers, we take this residual vector and compute its projection w.r.t. the 57 eigenvectors mentioned in Section 5.3, and subtract them off. This effectively erases information along these 57 eigenvectors from the residual vector. Finally, this residual vector is sliced to keep only the relevant sections, and is used with the sliced covariance matrix for fitting.

Now the best-fit cosmological parameters between a subset and the full dataset are finally comparable. Similar to Dutcher et al. [2021], we quantify their consistency with a parameter-level χ^2 and PTE, over the five parameters $\ln(10^{10}A_\mathrm{s}), n_s, \Omega_b h^2, \Omega_c h^2$, and $100\theta_s$ (5 degrees

of freedom). τ is excluded here because they are all dominated by the same prior.

$$\chi^2 = \Delta p^T C_p^{-1} \Delta p, \tag{7.1}$$

where Δp is a vector of the difference in best-fit parameters between the subset and the full dataset, and C_p is the covariance of the parameter differences. From Gratton and Challinor [2020], C_p simply equals the difference of parameter-level covariance matrices between the subset and the full dataset. (Details about how to obtain parameter-level covariance matrices are in Appendix C.) The results are listed in Table 7.2, and all seven data splits are within the central 95% confidence interval $[2.5\%, 97.5\%]$.

Table 7.2: Parameter-level χ^2 and the associated PTE between each data split and the full dataset. The five parameters being compared are $\ln(10^{10}A_{\rm s}), n_s, \Omega_b h^2, \Omega_c h^2$, and $100\theta_s$.

Subset	χ^2	PTE
95 GHz	6.16	29.1%
150 GHz	2.80	73.1%
95 × 150	1.83	87.2%
TE	1.63	89.8%
EE	2.16	82.7%
$\ell < 1000$	9.87	7.9%
$\ell > 1000$	12.57	2.8%

The goodness of fit w.r.t ΛCDM is generally improved over H18, except the TE-only subset. The χ^2 of the best-fit ΛCDM theory curve to the SPTpol TE-only bandpowers is $\chi^2 = 238.11$ for 180 degrees of freedom (PTE of 0.002). (Details on how to estimate the number of d.o.f. in the fit are in Appendix D.) For all other subsets, the χ^2 PTE are > 0.1.

7.2   Comparison with H18

H18 had many unresolved curiosities, including internal tensions and poor fits to ΛCDM. In this work, we made many fixes, added more data volume, improved sensitivity, and removed more systematics. As a result, most of those curiosities went away, the goodness of fit to
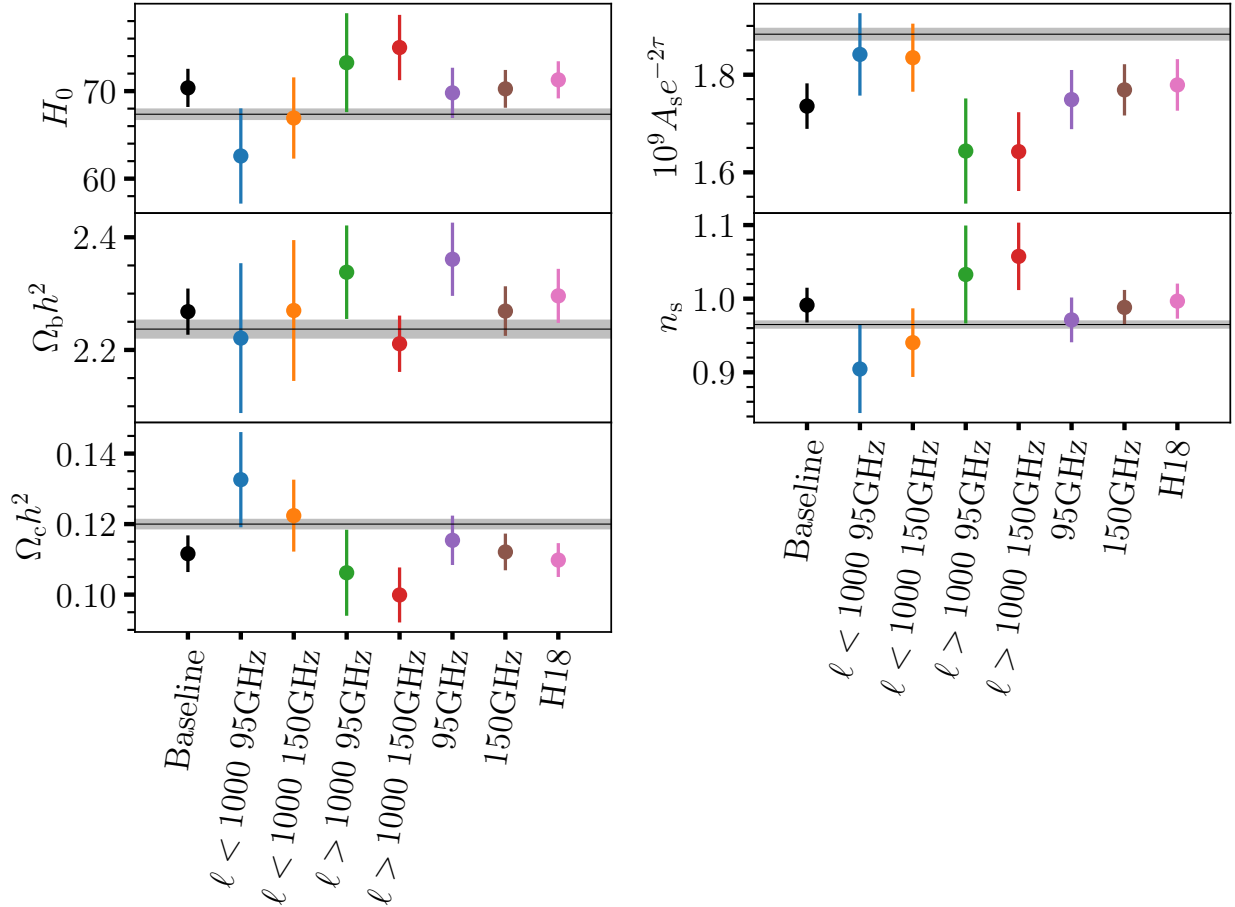
Figure 7.1: ΛCDM parameter constraints from the full SPTpol 500 deg^2 dataset (baseline), several data splits, and H18. For comparison, the horizontal lines and gray bands are the best-fit values and 1σ uncertainty ranges of *Planck*. These results are considered consistent but with a mild tension, where the $\ell < 1000$ and $\ell > 1000$ data splits pull in different directions for some of these parameters.

ΛCDM improved, and internal consistency between data splits and the full dataset are within the central 95% confidence interval. As a more apples-to-apples comparison to H18, we redo the ΛCDM fit of our 150 GHz-only subset, without the additional step of projecting w.r.t. the 57 eigenvectors as described in Section 7.1. The fit is indeed good, with $\chi^2 = 115.24$ for 104 degrees of freedom (PTE of 0.21). Further testing shows that this improvement in goodness of fit comes from improvements in the bandpowers, not the covariance matrix: When we redo this 150 GHz-only fit with our bandpowers and the covariance matrix of H18,

the fit is equally good (PTE of 0.21), but when we redo this fit with our covariance matrix and the bandpowers of H18, the $\chi^2 = 165.77$ for 104 degrees of freedom (PTE of 0.0001).

Despite these improvements, a curiosity persists from H18 to this work, namely the mild tension ($\sim 2\sigma$) in best-fit ΛCDM parameters between the $\ell < 1000$ and $\ell > 1000$ data split and the full dataset (the last two rows in Table 7.2). These two tensions are virtually two sides of the same coin, since the correlation between the $\ell < 1000$ and $\ell > 1000$ data subsets are negligible. In our work this tension is only mild, and H18 did not quantify this tension with a χ^2 PTE value either, but we still find it noteworthy to lay out the best-fit parameters in the same way for comparison. Columns (a), (b), (d), and (e) in Table 7.1 are ΛCDM fits to our data subsets without the additional step of projecting w.r.t. the 57 eigenvectors. Therefore, columns (b) and (d) are directly comparable with Table 4 in H18. For the purposes of obtaining best possible ΛCDM constraints here, we do not need to project out information along those 57 eigenvectors anyway, because the covariance matrices here have no numerical stability concerns. The dimensions are smaller, there are no nearly-identical rows because these are all single-frequency data subsets, and indeed we find no evidence of numerical issues with the covariance matrix of H18 when we used it in the previous paragraph.

Figure 7.1 plots the parameter constraints in Table 7.1 and some additional data (sub)sets. The trend seen in H18 persists, where the low-ℓ subset prefers a low H_0 and the high-ℓ subset prefers a high H_0. This is true for both the 95 GHz-only and the 150 GHz-only subsets. For the 150 GHz-only subsets (columns (b) and (d)), our ΛCDM parameter constraints are similar to those in H18. These suggest that the high / low-ℓ preference is a real feature on this 500 deg^2 patch of sky, however we note that SPT-3G 1500 deg^2 analyses [Dutcher et al., 2021, Balkenhol et al., 2023] do not see this trend.

The other possible explanation for this trend, is an uncaught systematic bias that is present in all our data subsets, yet somehow never degrades the goodness of fits. Some

potential sources of systematics were already ruled out in the jackknife null tests, and some others are being modeled as nuisance parameters. If we multiply the widths of the priors on the beam covariance nuisance parameters by a factor of 10, the χ^2 to the best-fit SPTpol cosmology changes by only -1.6. This suggests that our beam uncertainty modes are not driving the cosmological fits. Another test we perform is to restrict our data to $\ell < 3000$, same as SPT-3G analyses, in order to determine whether extragalactic point-source power at high ℓ caused these findings to be different between SPT-3G and SPTpol. The result is that the best-fit ΛCDM parameters change negligibly, ($\sim 0.07\sigma$ in the worst case,) therefore we conclude our model of the point-source power is also adequate. Lastly, Galactic foregrounds are also unlikely to be an unmodeled systematic contaminating our dataset. As pointed out by H18, the level of EE power from Galactic dust expected in our survey field is a factor of ~ 20 below our measured EE power in the lowest ℓ bin.
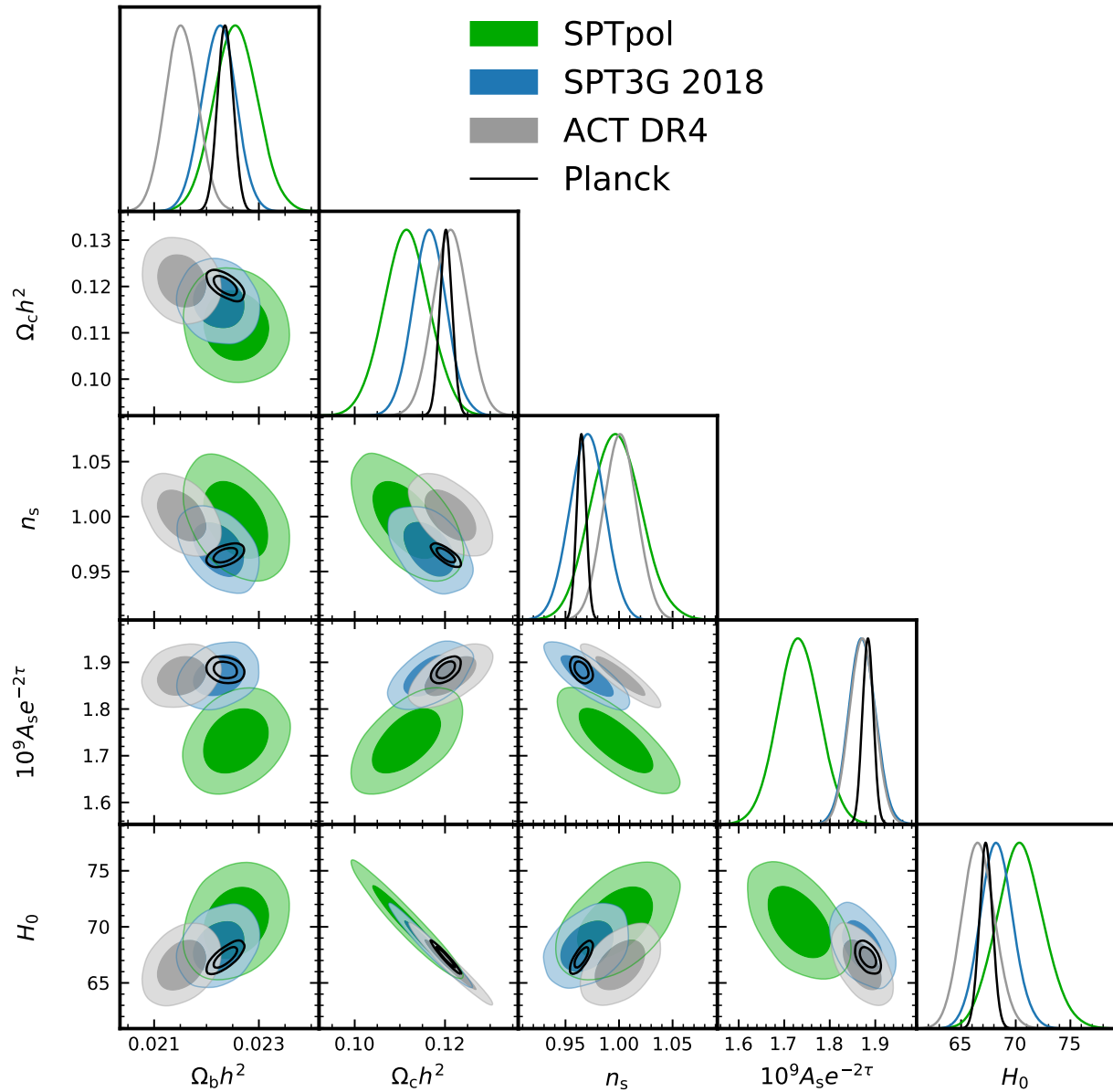
7.3   Comparison with other datasets

Figure 7.2 shows the marginalized ΛCDM parameter constraints (posteriors) for this work and other contemporary experiments. These constraints are in good agreement except for the parameter $10^9 A_s e^{-2\tau}$, where the constraints in this work have a $\gtrsim 3\sigma$ tension with *Planck*. As Figure 7.1 shows, the $10^9 A_s e^{-2\tau}$ constraints from the $\ell < 1000$ data splits in this work are actually consistent with *Planck*, and this tension is primarily driven by the $\ell > 1000$ data splits.

This is again reminiscent of H18, where they found a preference for the artificial scaling of lensing spectrum A_L to be lower than unity. CMB lensing causes peak smoothing and transfers power to the damping tail, and if A_L is lower than the expected value of one, the amplitude $10^9 A_s e^{-2\tau}$ measured from the $\ell > 1000$ subset will also be lower than expected. On the other hand, we expect our $\ell < 1000$ subset to show better agreement with *Planck*, because we calibrate the amplitudes of our power spectra (T_{cal} and P_{cal}) against *Planck* at

low ℓ.

We take the same approach as H18 and fit the extended model $\Lambda CDM + A_L$ to our full dataset. We find $A_L = 0.70 \pm 0.13$, which is lower than H18 ($A_L = 0.81 \pm 0.14$) and further away from one. When marginalized over A_L, the constraints for $10^9 A_s e^{-2\tau}$ and other ΛCDM parameters indeed shift closer to the values of *Planck*, and this tension is resolved. Furthermore, by fixing A_L to 0.7 instead of unity, the ΛCDM parameter constraints for the 150 GHz $\ell < 1000$ data split don't change much, but the constraints for 150 GHz $\ell > 1000$ move closer to the former (Figure 7.3). With A_L fixed to 0.7, the constraints on ΛCDM parameters agree between the 150 GHz $\ell < 1000$ and $\ell > 1000$ data splits, the full data, and *Planck*. We conclude that the aforementioned high / low-ℓ curiosity can be translated into the A_L curiosity instead, which is also at a $\sim 2\sigma$ level.

Figure 7.2: Marginalized ΛCDM parameter constraints (posteriors) for SPTpol (this work, green), SPT-3G 2018 $TT/TE/EE$ (blue)[Balkenhol et al., 2023], ACT DR4 (gray)[Aiola et al., 2020], and *Planck* (black line contours). The constraints for $10^9 A_s e^{-2\tau}$ in this work is in tension with those in other datasets.
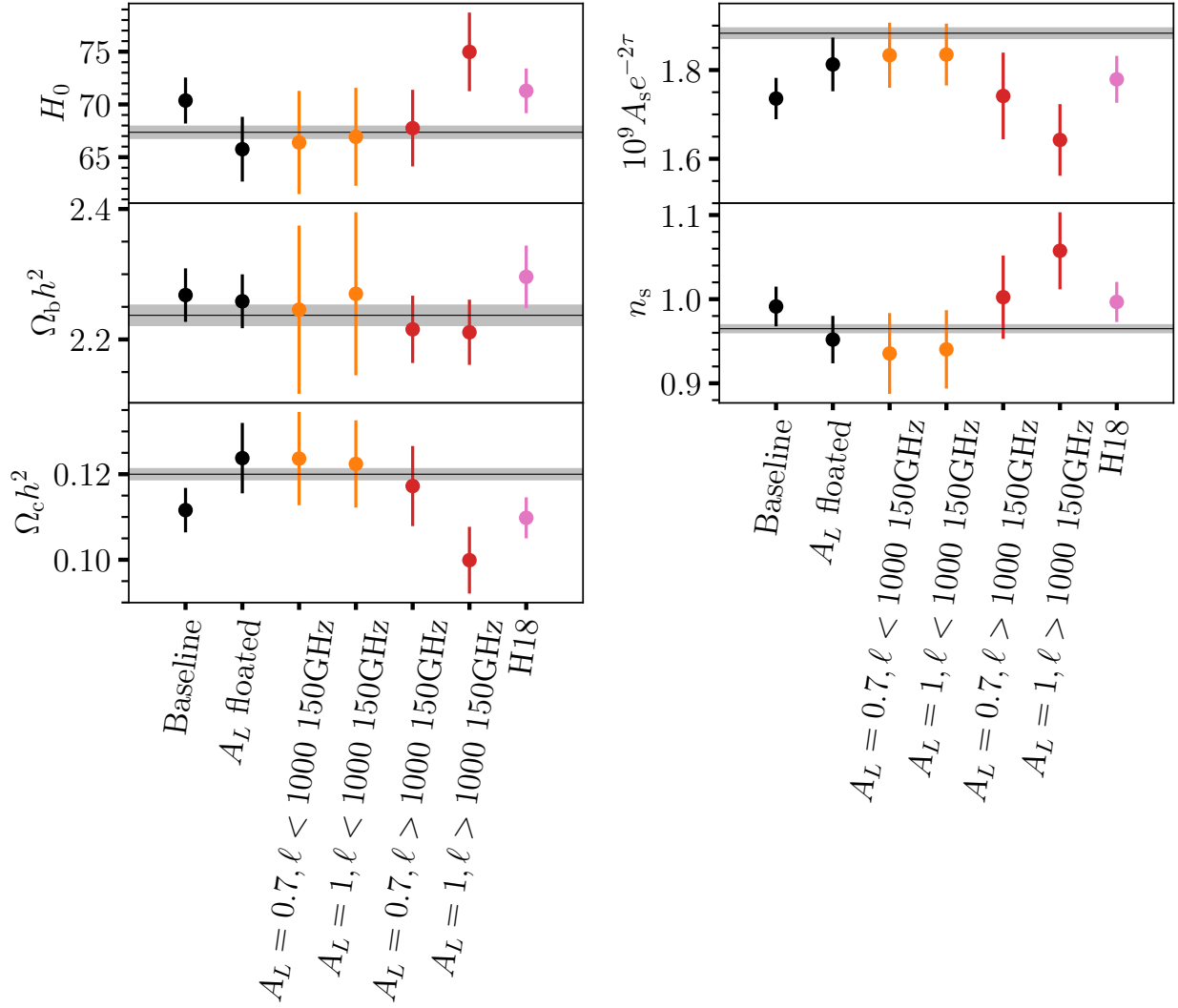
Figure 7.3: Constraints on ΛCDM parameters for the baseline, the full dataset but with A_L floated, the 150 GHz $\ell < 1000$ and $\ell > 1000$ data splits with A_L fixed to 0.7 or unity, and H18. The horizontal lines and gray bands are the best-fit values and 1σ uncertainty ranges of *Planck*. When A_L is fixed to 0.7, all these constraints agree between the 150 GHz $\ell < 1000$ and $\ell > 1000$ data splits, the full data, and *Planck*.

CHAPTER 8

CONCLUSION

We have presented the full four-year SPTpol 500 $\deg^2$ temperature and E-mode polarization maps, in both the 95 GHz and the 150 GHz frequency bands. We have also presented the TE and EE angular power spectra in the multipole range $50 < \ell < 8000$, and they are the most sensitive measurements of the CMB damping tail to date for roughly $\ell > 1700$ in TE and $\ell > 2000$ in EE.

This SPTpol dataset is self-consistent. The various cross-frequency bandpowers are consistent with each other, as evidenced by the chi-squared test on the minimum-variance bandpowers. The ΛCDM parameter constraints for 95 GHz and 150 GHz are also consistent with each other and with that of the full dataset. In contrast to H18, this dataset is a good fit to the ΛCDM model, as are most data splits in this work. The ΛCDM parameter constraints for every data split are all consistent with that of the full dataset.

Despite these improvements, a curiosity persists from H18 to this work. The ΛCDM parameter constraints between the $\ell < 1000$ and $\ell > 1000$ data splits are considered consistent but in mild tension ($\lesssim 2\sigma$). The Hubble constant H_0 for example, is 66.93 ± 4.64 km s^{-1} Mpc^{-1} for the 150 GHz $\ell < 1000$ data split, but 74.98 ± 3.73 km s^{-1} Mpc^{-1} for the 150 GHz $\ell > 1000$ data split. The same trend is seen in the 95 GHz $\ell < 1000$ vs. $\ell > 1000$ data splits. These suggest that the high / low-ℓ preference is a real feature on this 500 $\deg^2$ patch of sky, unless it is caused by an uncaught systematic bias that is present in all these data subsets yet never degrades the goodness of fits. However, we note that this trend is not seen in SPT-3G 1500 $\deg^2$ analyses [Dutcher et al., 2021, Balkenhol et al., 2023], therefore it is unlikely to be a hint for physics beyond ΛCDM.

As with H18, there is a preference for the artificial scaling of lensing spectrum A_L to be lower than unity. When we fit our full bandpowers with the extended model $\Lambda CDM + A_L$, we find $A_L = 0.70 \pm 0.13$, which is lower than H18 ($A_L = 0.81 \pm 0.14$) and further away

from one. This is the main reason that some of our parameter constraints appear different from *Planck*: In the base ΛCDM model, our A_s is significantly lower than *Planck*, but when we fit our data with the $\Lambda CDM + A_L$ extended model, our marginalized ΛCDM parameter constraints become consistent with *Planck*. With A_L fixed to 0.7, the constraints on ΛCDM parameters agree between the 150 GHz $\ell < 1000$ and $\ell > 1000$ data splits, the full data, and *Planck*. We conclude that the A_L curiosity is another way to represent the aforementioned high / low-ℓ curiosity, which is also at a $\sim 2\sigma$ level. We note that the SPT-3G 2018 $TT/TE/EE$ analysis also mildly prefers a low value of $A_L = 0.87 \pm 0.11$ [Balkenhol et al., 2023], which makes it an interesting topic for future studies.

We hope to learn more about these curiosities with upcoming analyses, such as the SPT-3G 2-year power spectrum analysis, SPT-3G full-dataset analysis, and ACT DR6. Future experiments such as CMB-S4 [CMB-S4 Collaboration, 2019] and Simons Observatory [Simons Observatory Collaboration, 2019] will provide even higher sensitivity measurements of the damping tail, and give us a better picture of the high-ℓ peaks.

APPENDIX A

MODELING AND VALIDATION OF THE 95 GHZ BEAM FUNCTION

As mentioned in Section 4.4, we find map artifacts in 95 GHz Venus observations. They contain a horizontal stripe structure (Figure A.1); the separation of these stripes is 0.5 arcminute, which is exactly the size of an elevation step in Venus observations, and it corresponds to a multipole $\ell = 43200$, which is way above the ℓ ranges that we report. Although the beam function in our ℓ range ($50 < \ell < 8000$) should be unaffected by these stripes, we worry that it might be indicative of a larger underlying problem, therefore it is still valuable to investigate this issue. Unfortunately, attempts to fix these Venus observations were unsuccessful. We suspected the calibration of certain bolometers being wrong, we found positive cross-talk between some bolometers, and we found that the "template" map (which our Venus maps were made upon) already contained these stripes. However, fixing these issues did not make these stripes go away much at all.

As a point of reference, we turn to making maps from Mars observations taken in 2012. The Mars maps do not suffer from this horizontal-stripe problem as the Venus maps do, so their beam function at high ℓ can be considered to be correct. A total of 9 Mars maps are made; one detail is that, as with our Venus maps, we need to first "blur" each Mars map so that its final size matches the size of pointing jitter in our 500 deg^2 field. We fit a 2D Gaussian to each Mars map to measure its size (σ_x, σ_y), and then convolve each map with another 2D Gaussian whose σ_x and σ_y are the quadrature difference of the pointing jitter and this previously measured size. Then we compute their cross-spectra in the usual way to obtain the beam function B_ℓ of Mars. Finally, we compare the B_ℓ^2 between Mars and Venus by computing their ratio. The result is that Venus and Mars only differ by a few percent in the range $1000 < \ell < 8000$, which suggests Venus B_ℓ is actually reasonable, and not "the tip of an iceberg" of any bigger underlying problem. A beam uncertainty of a few percent
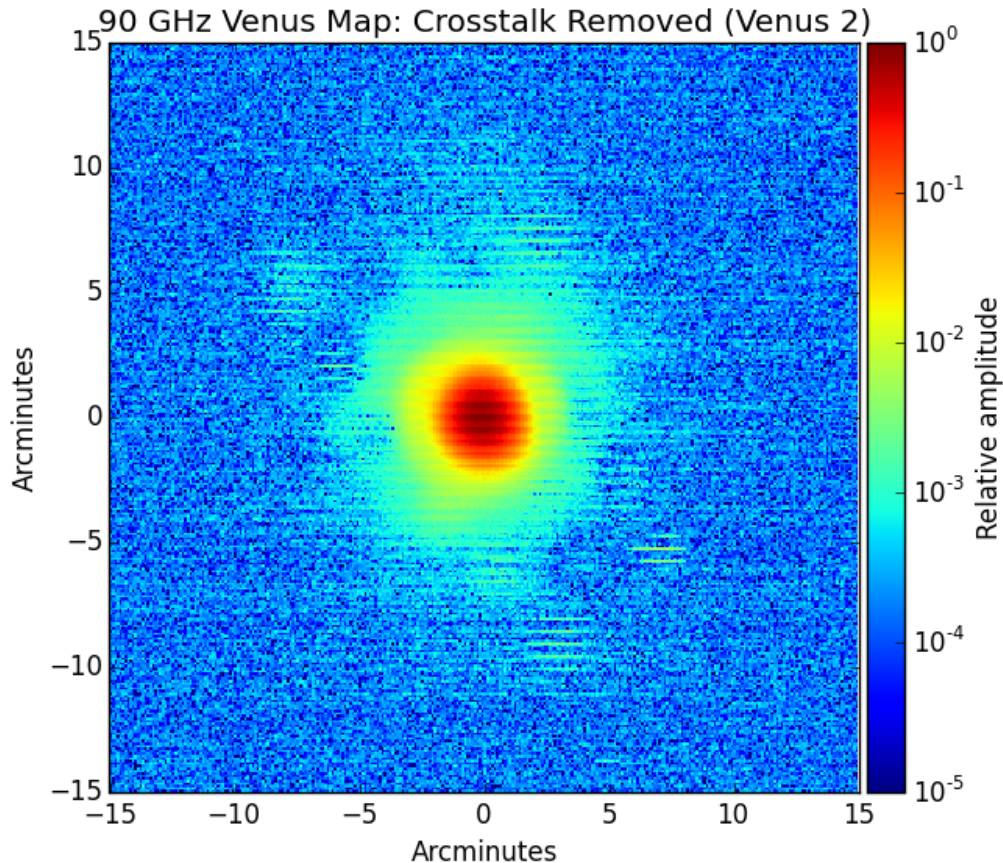
Figure A.1: A 95 GHz Venus observation. There is a clear horizontal stripe structure that contaminates the beam function at very high ℓ ranges.

is expected and indeed accounted for when we modeled the beam uncertainty, whether as a covariance matrix or as nuisance parameters in the cosmology fits.

We continue to use Venus maps to compute B_ℓ because they have better sensitivity at low ℓ. (Mars is too dim, the B_ℓ measured from Mars is unusable for $\ell < 1000$.) In our final product, we only use 5 Venus observations, where H18 used 7; we cut more observations because in this work they have to be well-behaved in both 95 and 150 GHz bands at the same time, in order for us to compute the 95×150 beam function. These Venus B_ℓ are then used in the calibrations and fits against *Planck* as described in Section 4.4.

APPENDIX B

COMBINING THE LOW-ℓ AND HIGH-ℓ FOCUSED BANDPOWERS

In this work we process the data into two sets of bandpowers, a low-ℓ focused one and a high-ℓ focused one, and we choose to stitch them at $\ell = 500$. The choice of this ℓ value is motivated by limitations from either side.

First, the low-ℓ focused maps are made with $3'$-pixels, and when converted to the angular power spectrum, they correspond to an Nyquist ℓ of 3600. We apply a lowpass filter on the time streams at $\ell = 3200$, so at least along the scan direction there should be negligible aliasing at $\ell \sim 1000$. However, as a sanity check we compute the ratio of EE power spectrum between a $3'$-pixelization and a $0.5'$-pixelization, using the 500 sets of simulated bandpowers from our mock-observations. The bandpowers from $0.5'$-pixel maps are considered "the truth" that do not contain aliased power. We expect the bandpowers from $3'$-pixel maps to agree with them, but we find noticeable aliasing as shown in Figure B.1. The error bars represent the sample variance between these 500 sets of bandpowers, and above roughly $\ell > 600$ this aliased power becomes greater than the sample variance. We conclude that we should not use bandpowers from the low-ℓ focused maps above $\ell > 600$.

On the other hand, the high-ℓ focused dataset has a highpass filter at $\ell = 300$ and a common mode filter that is an effective highpass at $\ell \sim 360$. As ℓ increases, the filter transfer functions ramp up as shown in Figure B.2. A low transfer function would lead to a low signal-to-noise measurement; in addition, the unbiased power spectrum would be more sensitive to fluctuations in the estimated transfer function. Therefore we conclude that, for the range $\ell < 500$, the transfer function is too low to be satisfactory. Combining these two limitations, we finally choose to stitch at $\ell = 500$.
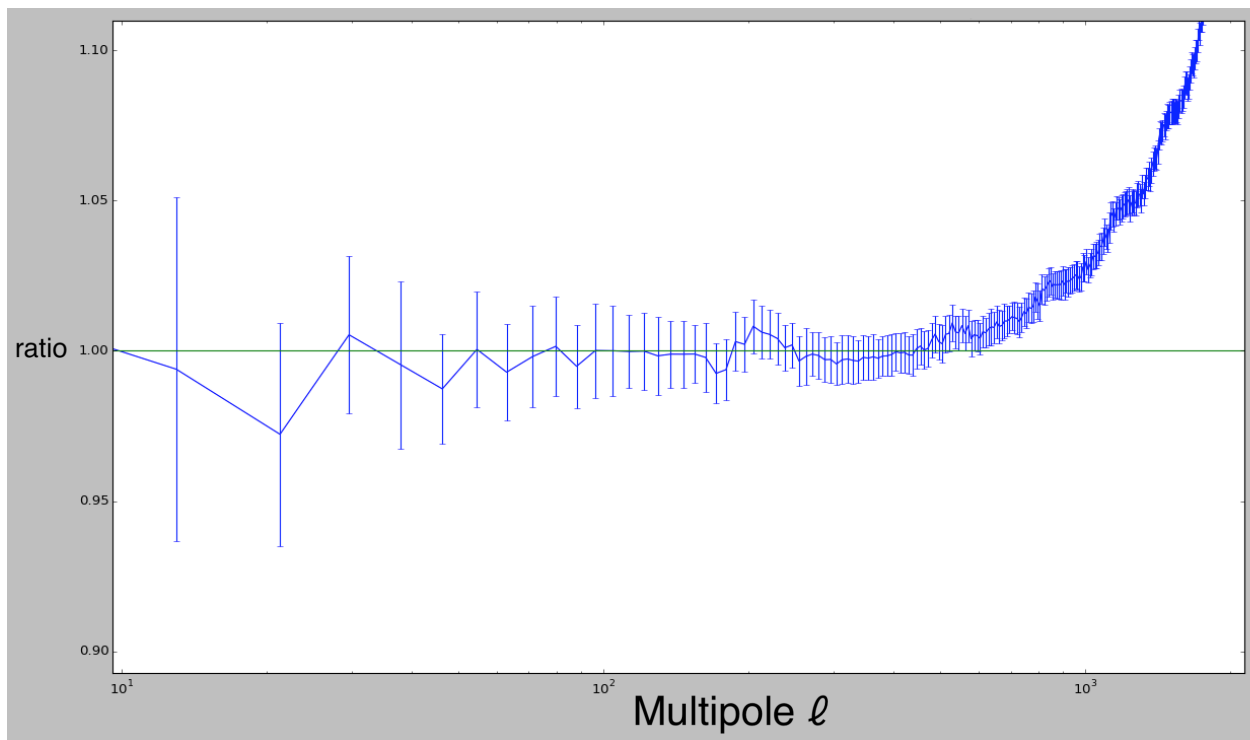
Figure B.1: Ratio of simulated EE power spectrum between a $3'$-pixelization and a $0.5'$-pixelization. The pixel window functions are already divided out in each case. Error bars represent the sample variance between these 500 sets of bandpowers.
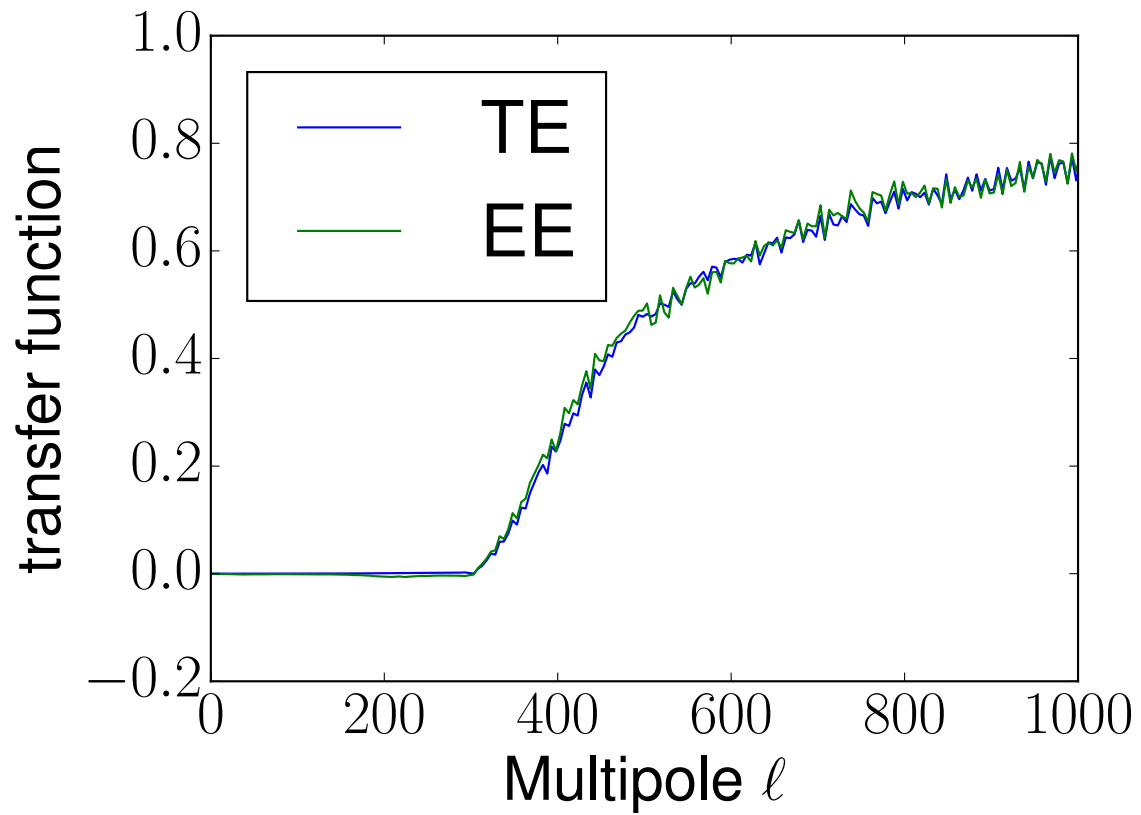
Figure B.2: 150 GHz filter transfer function for the high-ℓ focused dataset, for TE (blue) and EE (green).

APPENDIX C

COVARIANCE MATRICES BETWEEN COSMOLOGICAL PARAMETERS

In Section 7.1, we quantify the cosmological parameter constraints between each data split versus the full dataset. The difference in best-fit parameters between the subset and the full dataset is expected to follow a certain parameter-level covariance matrix C_p, and from analytical calculations in Gratton and Challinor [2020], C_p simply equals the difference of parameter-level covariance matrices between the subset and the full dataset.

In practice, we obtain parameter-level covariance matrices numerically from all the sample points in the Markov chain, then we obtain C_p by subtracting the covariance matrix of the full dataset from that of the subset. However, it is possible to run into numerical issues, due to an insufficient number of sample points, and/or strong degeneracy between cosmological parameters.

Initially, we tried using the same five ΛCDM parameters as in Dutcher et al. [2021]: $10^9 A_s e^{-2\tau}, n_s, \Omega_b h^2, \Omega_c h^2$, and $100\theta_s$. However, C_p for the $\ell > 1000$ data split was actually not positive-definite, and it resulted in a negative χ^2 value. This was a numerical issue, potentially due to the strong degeneracy between n_s and $10^9 A_s e^{-2\tau}$. We tried running the Markov chain longer for more sample points, but it still wasn't enough.

As a preliminary test, we tried only using four cosmological parameters at a time, either removing n_s or $10^9 A_s e^{-2\tau}$ from C_p. This worked and everything was well-behaved, but we still wanted a solution that involved all five parameters. Next, we swapped out the $10^9 A_s e^{-2\tau}$ parameter for $\ln(10^{10} A_s)$, the latter having a weaker degeneracy with n_s. This resolved the numerical issue, and resulted in a positive-definite C_p and a positive χ^2.

We made the parameter-level covariance matrices even more well-behaved by taking their average from our 226 simulated bandpowers. For each simulated set of bandpowers, we ran the usual MCMC fit, and made a parameter-level covariance matrix from the sample points.

We averaged together these 226 covariance matrices, which reduced its numerical noise even further, then finally inverted it to compute χ^2 in the usual way:

$$\chi^2 = \Delta p^T C_p^{-1} \Delta p,$$

Now everything is well-behaved and positive-definite, and the χ^2 and PTE results were already shown in table 7.2. As mentioned in the main text, the two mild tensions that the $\ell < 1000$ and $\ell > 1000$ data splits have compared to the full dataset (the last two rows in Table 7.2) are virtually two sides of the same coin, since the correlation between the $\ell < 1000$ and $\ell > 1000$ data subsets are negligible. These two tensions are actually describing the same tension, so their χ^2 values are expected to be similar, and we can see from the table that they indeed are. This also suggests that C_p is well-behaved.

APPENDIX D

ESTIMATION OF THE DEGREES OF FREEDOM FOR DATA SPLITS

We quantify the goodness of fit of each data split with respect to ΛCDM by comparing the best-fit χ^2 value to a certain number of d.o.f. Usually d.o.f. equals the number of bandpowers minus the number of free parameters that are not prior-dominated (there is a little room for subjectivity in judging which parameters are prior-dominated). But the situation for our data splits is even more complicated, because we project out 57 specific vectors from the residual vectors at every step in the Markov chain, which means the d.o.f. is reduced by some number between 0–57.

We choose to estimate the d.o.f. using our 226 simulated bandpowers. In the case of the full data vector (392 ℓ bins), when we take the simulated bandpowers, subtract their mean, and compute $\chi^2 = v^T \cdot C^{-1} \cdot v$ (where v is a vector of the bandpowers and C is the $7x7$-block bandpower covariance matrix), they should form a χ^2 distribution with $392 - 1 = 391$ d.o.f. And if 57 eigenvectors were projected out from the residual vectors at every step in the Markov chain, the d.o.f. becomes $392 - 1 - 57 = 334$. This was indeed one of the sanity checks that the covariance matrix had to pass during its construction and validation in Section 5.3.

Now for the data splits, we project out those 57 specific vectors in the same way, and in the last step, we slice the residual vectors and covariance matrices into smaller block ones, keeping only the relevant sections. Now the $\chi^2 = v^T \cdot C^{-1} \cdot v$ of our 226 simulated bandpowers should form a χ^2 distribution with d.o.f. equal to the number of bandpowers minus one minus some number between 0–57; this number is exactly what we want to measure here. Therefore we do this procedure twice, once with projecting out those 57 specific vectors, and once without. We take the average χ^2 value in each case, subtract them, and round to an integer. This becomes our estimate of the d.o.f. that were reduced for this data split.

As a result, the d.o.f. reduced by 0, 1, 4, 37, 26, 36, and 28 for the 95 GHz, 95×150, 150 GHz, TE, EE, $\ell < 1000$, and $\ell > 1000$ data splits, respectively. We subtract this value from the d.o.f. when calculating the goodness-of-fit χ^2 PTE values in Section 7.1.

REFERENCES

Simone Aiola, Erminia Calabrese, Loïc Maurin, Sigurd Naess, Benjamin L. Schmitt, Maximilian H. Abitbol, Graeme E. Addison, Peter A. R. Ade, David Alonso, Mandana Amiri, Stefania Amodeo, Elio Angile, Jason E. Austermann, Taylor Baildon, Nick Battaglia, James A. Beall, Rachel Bean, Daniel T. Becker, J. Richard Bond, Sarah Marie Bruno, Victoria Calafut, Luis E. Campusano, Felipe Carrero, Grace E. Chesmore, Hsiao-mei Cho, Steve K. Choi, Susan E. Clark, Nicholas F. Cothard, Devin Crichton, Kevin T. Crowley, Omar Darwish, Rahul Datta, Edward V. Denison, Mark J. Devlin, Cody J. Duell, Shannon M. Duff, Adriaan J. Duivenvoorden, Jo Dunkley, Rolando Dünner, Thomas Essinger-Hileman, Max Fankhanel, Simone Ferraro, Anna E. Fox, Brittany Fuzia, Patricio A. Gallardo, Vera Gluscevic, Joseph E. Golec, Emily Grace, Megan Gralla, Yilun Guan, Kirsten Hall, Mark Halpern, Dongwon Han, Peter Hargrave, Matthew Hasselfield, Jakob M. Helton, Shawn Henderson, Brandon Hensley, J. Colin Hill, Gene C. Hilton, Matt Hilton, Adam D. Hincks, Renée Hložek, Shuay-Pwu Patty Ho, Johannes Hubmayr, Kevin M. Huffenberger, John P. Hughes, Leopoldo Infante, Kent Irwin, Rebecca Jackson, Jeff Klein, Kenda Knowles, Brian Koopman, Arthur Kosowsky, Vincent Lakey, Dale Li, Yaqiong Li, Zack Li, Martine Lokken, Thibaut Louis, Marius Lungu, Amanda MacInnis, Mathew Madhavacheril, Felipe Maldonado, Maya Mallaby-Kay, Danica Marsden, Jeff McMahon, Felipe Menanteau, Kavilan Moodley, Tim Morton, Toshiya Namikawa, Federico Nati, Laura Newburgh, John P. Nibarger, Andrina Nicola, Michael D. Niemack, Michael R. Nolta, John Orlowski-Sherer, Lyman A. Page, Christine G. Pappas, Bruce Partridge, Phumlani Phakathi, Giampaolo Pisano, Heather Prince, Roberto Puddu, Frank J. Qu, Jesus Rivera, Naomi Robertson, Felipe Rojas, Maria Salatino, Emmanuel Schaan, Alessandro Schillaci, Neelima Sehgal, Blake D. Sherwin, Carlos Sierra, Jon Sievers, Cristobal Sifon, Precious Sikhosana, Sara Simon, David N. Spergel, Suzanne T. Staggs, Jason Stevens, Emilie Storer, Dhaneshwar D. Sunder, Eric R. Switzer, Ben Thorne, Robert Thornton, Hy Trac, Jesse Treu, Carole Tucker, Leila R. Vale, Alexander Van Engelen, Jeff Van Lanen, Eve M. Vavagiakis, Kasey Wagoner, Yuhan Wang, Jonathan T. Ward, Edward J. Wollack, Zhilei Xu, Fernando Zago, and Ningfeng Zhu. The Atacama Cosmology Telescope: DR4 maps and cosmological parameters. *JCAP*, 2020(12):047, December 2020. doi:10.1088/1475-7516/2020/12/047.

K. Aylor, Z. Hou, L. Knox, K. T. Story, B. A. Benson, L. E. Bleem, J. E. Carlstrom, C. L. Chang, H.-M. Cho, R. Chown, T. M. Crawford, A. T. Crites, T. de Haan, M. A. Dobbs, W. B. Everett, E. M. George, N. W. Halverson, N. L. Harrington, G. P. Holder, W. L. Holzapfel, J. D. Hrubes, R. Keisler, A. T. Lee, E. M. Leitch, D. Luong-Van, D. P. Marrone, J. J. McMahon, S. S. Meyer, M. Millea, L. M. Mocanu, J. J. Mohr, T. Natoli, Y. Omori, S. Padin, C. Pryke, C. L. Reichardt, J. E. Ruhl, J. T. Sayre, K. K. Schaffer, E. Shirokoff, Z. Staniszewski, A. A. Stark, K. Vanderlinde, J. D. Vieira, and R. Williamson. A Comparison of Cosmological Parameters Determined from CMB Temperature Power Spectra from the South Pole Telescope and the Planck Satellite. *ApJ*, 850:101, November 2017. doi:10.3847/1538-4357/aa947b.

L. Balkenhol, D. Dutcher, A. Spurio Mancini, A. Doussot, K. Benabed, S. Galli, P. A. R. Ade,

A. J. Anderson, B. Ansarinejad, M. Archipley, A. N. Bender, B. A. Benson, F. Bianchini, L. E. Bleem, F. R. Bouchet, L. Bryant, E. Camphuis, J. E. Carlstrom, T. W. Cecil, C. L. Chang, P. Chaubal, P. M. Chichura, T. L. Chou, A. Coerver, T. M. Crawford, A. Cukierman, C. Daley, T. de Haan, K. R. Dibert, M. A. Dobbs, W. Everett, C. Feng, K. R. Ferguson, A. Foster, A. E. Gambrel, R. W. Gardner, N. Goeckner-Wald, R. Gualtieri, F. Guidi, S. Guns, N. W. Halverson, E. Hivon, G. P. Holder, W. L. Holzapfel, J. C. Hood, N. Huang, L. Knox, M. Korman, C. L. Kuo, A. T. Lee, A. E. Lowitz, C. Lu, M. Millea, J. Montgomery, Y. Nakato, T. Natoli, G. I. Noble, V. Novosad, Y. Omori, S. Padin, Z. Pan, P. Paschos, K. Prabhu, W. Quan, M. Rahimi, A. Rahlin, C. L. Reichardt, M. Rouble, J. E. Ruhl, E. Schiappucci, G. Smecher, J. A. Sobrin, A. A. Stark, J. Stephen, A. Suzuki, C. Tandoi, K. L. Thompson, B. Thorne, C. Tucker, C. Umilta, J. D. Vieira, G. Wang, N. Whitehorn, W. L. K. Wu, V. Yefremenko, M. R. Young, J. A. Zebrowski, and SPT-3G Collaboration. Measurement of the CMB temperature power spectrum and constraints on cosmology from the SPT-3G 2018 T T , T E , and E E dataset. *PhRvD*, 108(2):023510, July 2023. doi:10.1103/PhysRevD.108.023510.

A. Benoit-Lévy, K. M. Smith, and W. Hu. Non-Gaussian structure of the lensed CMB power spectra covariance matrix. *PhRvD*, 86(12):123008, December 2012. doi:10.1103/PhysRevD.86.123008.

BICEP2 and Keck Array Collaborations, P. A. R. Ade, Z. Ahmed, R. W. Aikin, K. D. Alexander, D. Barkats, S. J. Benton, C. A. Bischoff, J. J. Bock, J. A. Brevik, I. Buder, E. Bullock, V. Buza, J. Connors, B. P. Crill, C. D. Dowell, C. Dvorkin, L. Duband, J. P. Filippini, S. Fliescher, S. R. Golwala, M. Halpern, S. Harrison, M. Hasselfield, S. R. Hildebrandt, G. C. Hilton, V. V. Hristov, H. Hui, K. D. Irwin, K. S. Karkare, J. P. Kaufman, B. G. Keating, S. Kefeli, S. A. Kernasovskiy, J. M. Kovac, C. L. Kuo, E. M. Leitch, M. Lueker, P. Mason, K. G. Megerian, C. B. Netterfield, H. T. Nguyen, R. O'Brient, IV Ogburn, R. W., A. Orlando, C. Pryke, C. D. Reintsema, S. Richter, R. Schwarz, C. D. Sheehy, Z. K. Staniszewski, R. V. Sudiwala, G. P. Teply, K. L. Thompson, J. E. Tolan, A. D. Turner, A. G. Vieregg, A. C. Weber, J. Willmert, C. L. Wong, and K. W. Yoon. BICEP2/Keck Array V: Measurements of B-mode Polarization at Degree Angular Scales and 150 GHz by the Keck Array. *ApJ*, 811(2):126, October 2015. doi:10.1088/0004-637X/811/2/126.

Diego Blas, Julien Lesgourgues, and Thomas Tram. The Cosmic Linear Anisotropy Solving System (CLASS). Part II: Approximation schemes. *JCAP*, 2011(7):034, July 2011. doi:10.1088/1475-7516/2011/07/034.

Boris Bolliet, Alessio Spurio Mancini, J. Colin Hill, Mathew Madhavacheril, Hidde T. Jense, Erminia Calabrese, and Jo Dunkley. High-accuracy emulators for observables in ΛCDM, N_{eff}, Σm_ν, and w cosmologies. *arXiv e-prints*, art. arXiv:2303.01591, March 2023. doi:10.48550/arXiv.2303.01591.

J. E. Carlstrom, P. A. R. Ade, K. A. Aird, B. A. Benson, L. E. Bleem, S. Busetti, C. L. Chang, E. Chauvin, H.-M. Cho, T. M. Crawford, A. T. Crites, M. A. Dobbs, N. W.

Halverson, S. Heimsath, W. L. Holzapfel, J. D. Hrubes, M. Joy, R. Keisler, T. M. Lanting, A. T. Lee, E. M. Leitch, J. Leong, W. Lu, M. Lueker, D. Luong-van, J. J. McMahon, J. Mehl, S. S. Meyer, J. J. Mohr, T. E. Montroy, S. Padin, T. Plagge, C. Pryke, J. E. Ruhl, K. K. Schaffer, D. Schwan, E. Shirokoff, H. G. Spieler, Z. Staniszewski, A. A. Stark, C. Tucker, K. Vanderlinde, J. D. Vieira, and R. Williamson. The 10 Meter South Pole Telescope. *PASP*, 123:568–581, May 2011. doi:10.1086/659879.

Steve K. Choi, Matthew Hasselfield, Shuay-Pwu Patty Ho, Brian Koopman, Marius Lungu, Maximilian H. Abitbol, Graeme E. Addison, Peter A. R. Ade, Simone Aiola, David Alonso, Mandana Amiri, Stefania Amodeo, Elio Angile, Jason E. Austermann, Taylor Baildon, Nick Battaglia, James A. Beall, Rachel Bean, Daniel T. Becker, J. Richard Bond, Sarah Marie Bruno, Erminia Calabrese, Victoria Calafut, Luis E. Campusano, Felipe Carrero, Grace E. Chesmore, Hsiao-mei Cho, Susan E. Clark, Nicholas F. Cothard, Devin Crichton, Kevin T. Crowley, Omar Darwish, Rahul Datta, Edward V. Denison, Mark J. Devlin, Cody J. Duell, Shannon M. Duff, Adriaan J. Duivenvoorden, Jo Dunkley, Rolando Dünner, Thomas Essinger-Hileman, Max Fankhanel, Simone Ferraro, Anna E. Fox, Brittany Fuzia, Patricio A. Gallardo, Vera Gluscevic, Joseph E. Golec, Emily Grace, Megan Gralla, Yilun Guan, Kirsten Hall, Mark Halpern, Dongwon Han, Peter Hargrave, Shawn Henderson, Brandon Hensley, J. Colin Hill, Gene C. Hilton, Matt Hilton, Adam D. Hincks, Renée Hložek, Johannes Hubmayr, Kevin M. Huffenberger, John P. Hughes, Leopoldo Infante, Kent Irwin, Rebecca Jackson, Jeff Klein, Kenda Knowles, Arthur Kosowsky, Vincent Lakey, Dale Li, Yaqiong Li, Zack Li, Martine Lokken, Thibaut Louis, Amanda MacInnis, Mathew Madhavacheril, Felipe Maldonado, Maya Mallaby-Kay, Danica Marsden, Loïc Maurin, Jeff McMahon, Felipe Menanteau, Kavilan Moodley, Tim Morton, Sigurd Naess, Toshiya Namikawa, Federico Nati, Laura Newburgh, John P. Nibarger, Andrina Nicola, Michael D. Niemack, Michael R. Nolta, John Orlowski-Sherer, Lyman A. Page, Christine G. Pappas, Bruce Partridge, Phumlani Phakathi, Heather Prince, Roberto Puddu, Frank J. Qu, Jesus Rivera, Naomi Robertson, Felipe Rojas, Maria Salatino, Emmanuel Schaan, Alessandro Schillaci, Benjamin L. Schmitt, Neelima Sehgal, Blake D. Sherwin, Carlos Sierra, Jon Sievers, Cristobal Sifon, Precious Sikhosana, Sara Simon, David N. Spergel, Suzanne T. Staggs, Jason Stevens, Emilie Storer, Dhaneshwar D. Sunder, Eric R. Switzer, Ben Thorne, Robert Thornton, Hy Trac, Jesse Treu, Carole Tucker, Leila R. Vale, Alexander Van Engelen, Jeff Van Lanen, Eve M. Vavagiakis, Kasey Wagoner, Yuhan Wang, Jonathan T. Ward, Edward J. Wollack, Zhilei Xu, Fernando Zago, and Ningfeng Zhu. The Atacama Cosmology Telescope: a measurement of the Cosmic Microwave Background power spectra at 98 and 150 GHz. *JCAP*, 2020(12):045, December 2020. doi:10.1088/1475-7516/2020/12/045.

CMB-S4 Collaboration. CMB-S4 Science Case, Reference Design, and Project Plan. *arXiv e-prints*, art. arXiv:1907.04473, Jul 2019.

A. T. Crites, J. W. Henning, P. A. R. Ade, K. A. Aird, J. E. Austermann, J. A. Beall, A. N. Bender, B. A. Benson, L. E. Bleem, J. E. Carlstrom, C. L. Chang, H. C. Chiang, H.-M. Cho, R. Citron, T. M. Crawford, T. de Haan, M. A. Dobbs, W. Everett, J. Gallicchio, J. Gao, E. M. George, A. Gilbert, N. W. Halverson, D. Hanson, N. Harrington,

G. C. Hilton, G. P. Holder, W. L. Holzapfel, S. Hoover, Z. Hou, J. D. Hrubes, N. Huang, J. Hubmayr, K. D. Irwin, R. Keisler, L. Knox, A. T. Lee, E. M. Leitch, D. Li, C. Liang, D. Luong-Van, J. J. McMahon, J. Mehl, S. S. Meyer, L. Mocanu, T. E. Montroy, T. Natoli, J. P. Nibarger, V. Novosad, S. Padin, C. Pryke, C. L. Reichardt, J. E. Ruhl, B. R. Saliwanchik, J. T. Sayre, K. K. Schaffer, G. Smecher, A. A. Stark, K. T. Story, C. Tucker, K. Vanderlinde, J. D. Vieira, G. Wang, N. Whitehorn, V. Yefremenko, and O. Zahn. Measurements of E-Mode Polarization and Temperature-E-Mode Correlation in the Cosmic Microwave Background from 100 Square Degrees of SPTpol Data. *ApJ*, 805:36, May 2015. doi:10.1088/0004-637X/805/1/36.

D. Dutcher, L. Balkenhol, P. A. R. Ade, Z. Ahmed, E. Anderes, A. J. Anderson, M. Archipley, J. S. Avva, K. Aylor, P. S. Barry, R. Basu Thakur, K. Benabed, A. N. Bender, B. A. Benson, F. Bianchini, L. E. Bleem, F. R. Bouchet, L. Bryant, K. Byrum, J. E. Carlstrom, F. W. Carter, T. W. Cecil, C. L. Chang, P. Chaubal, G. Chen, H. M. Cho, T. L. Chou, J. F. Cliche, T. M. Crawford, A. Cukierman, C. Daley, T. de Haan, E. V. Denison, K. Dibert, J. Ding, M. A. Dobbs, W. Everett, C. Feng, K. R. Ferguson, A. Foster, J. Fu, S. Galli, A. E. Gambrel, R. W. Gardner, N. Goeckner-Wald, R. Gualtieri, S. Guns, N. Gupta, R. Guyser, N. W. Halverson, A. H. Harke-Hosemann, N. L. Harrington, J. W. Henning, G. C. Hilton, E. Hivon, G. P. Holder, W. L. Holzapfel, J. C. Hood, D. Howe, N. Huang, K. D. Irwin, O. B. Jeong, M. Jonas, A. Jones, T. S. Khaire, L. Knox, A. M. Kofman, M. Korman, D. L. Kubik, S. Kuhlmann, C. L. Kuo, A. T. Lee, E. M. Leitch, A. E. Lowitz, C. Lu, S. S. Meyer, D. Michalik, M. Millea, J. Montgomery, A. Nadolski, T. Natoli, H. Nguyen, G. I. Noble, V. Novosad, Y. Omori, S. Padin, Z. Pan, P. Paschos, J. Pearson, C. M. Posada, K. Prabhu, W. Quan, S. Raghunathan, A. Rahlin, C. L. Reichardt, D. Riebel, B. Riedel, M. Rouble, J. E. Ruhl, J. T. Sayre, E. Schiappucci, E. Shirokoff, G. Smecher, J. A. Sobrin, A. A. Stark, J. Stephen, K. T. Story, A. Suzuki, K. L. Thompson, B. Thorne, C. Tucker, C. Umilta, L. R. Vale, K. Vanderlinde, J. D. Vieira, G. Wang, N. Whitehorn, W. L. K. Wu, V. Yefremenko, K. W. Yoon, M. R. Young, and SPT-3G Collaboration. Measurements of the E -mode polarization and temperature-E -mode correlation of the CMB from SPT-3G 2018 data. *PhRvD*, 104(2):022003, July 2021. doi:10.1103/PhysRevD.104.022003.

S. Galli, K. Benabed, F. Bouchet, J.-F. Cardoso, F. Elsner, E. Hivon, A. Mangilli, S. Prunet, and B. Wandelt. CMB polarization can constrain cosmology better than CMB temperature. *PhRvD*, 90(6):063504, September 2014. doi:10.1103/PhysRevD.90.063504.

K. M. Górski, E. Hivon, A. J. Banday, B. D. Wandelt, F. K. Hansen, M. Reinecke, and M. Bartelmann. HEALPix: A Framework for High-Resolution Discretization and Fast Analysis of Data Distributed on the Sphere. *ApJ*, 622:759–771, April 2005. doi:10.1086/427976.

Steven Gratton and Anthony Challinor. Understanding parameter differences between analyses employing nested data subsets. *MNRAS*, 499(3):3410–3416, December 2020. doi:10.1093/mnras/staa2996.

J. W. Henning, J. T. Sayre, C. L. Reichardt, P. A. R. Ade, A. J. Anderson, J. E. Austermann, J. A. Beall, A. N. Bender, B. A. Benson, L. E. Bleem, J. E. Carlstrom, C. L. Chang, H. C.

Chiang, H.-M. Cho, R. Citron, C. Corbett Moran, T. M. Crawford, A. T. Crites, T. de Haan, M. A. Dobbs, W. Everett, J. Gallicchio, E. M. George, A. Gilbert, N. W. Halverson, N. Harrington, G. C. Hilton, G. P. Holder, W. L. Holzapfel, S. Hoover, Z. Hou, J. D. Hrubes, N. Huang, J. Hubmayr, K. D. Irwin, R. Keisler, L. Knox, A. T. Lee, E. M. Leitch, D. Li, A. Lowitz, A. Manzotti, J. J. McMahon, S. S. Meyer, L. Mocanu, J. Montgomery, A. Nadolski, T. Natoli, J. P. Nibarger, V. Novosad, S. Padin, C. Pryke, J. E. Ruhl, B. R. Saliwanchik, K. K. Schaffer, C. Sievers, G. Smecher, A. A. Stark, K. T. Story, C. Tucker, K. Vanderlinde, T. Veach, J. D. Vieira, G. Wang, N. Whitehorn, W. L. K. Wu, and V. Yefremenko. Measurements of the Temperature and E-mode Polarization of the CMB from 500 Square Degrees of SPTpol Data. *ApJ*, 852:97, January 2018. doi:10.3847/1538-4357/aa9ff4.

Catherine Heymans, Tilman Tröster, Marika Asgari, Chris Blake, Hendrik Hildebrandt, Benjamin Joachimi, Konrad Kuijken, Chieh-An Lin, Ariel G. Sánchez, Jan Luca van den Busch, Angus H. Wright, Alexandra Amon, Maciej Bilicki, Jelte de Jong, Martin Crocce, Andrej Dvornik, Thomas Erben, Maria Cristina Fortuna, Fedor Getman, Benjamin Giblin, Karl Glazebrook, Henk Hoekstra, Shahab Joudaki, Arun Kannawadi, Fabian Köhlinger, Chris Lidman, Lance Miller, Nicola R. Napolitano, David Parkinson, Peter Schneider, HuanYuan Shan, Edwin A. Valentijn, Gijs Verdoes Kleijn, and Christian Wolf. KiDS-1000 Cosmology: Multi-probe weak gravitational lensing and spectroscopic galaxy clustering constraints. *A&A*, 646:A140, February 2021. doi:10.1051/0004-6361/202039063.

Eric Hivon, Krzysztof M. Górski, C. Barth Netterfield, Brendan P. Crill, Simon Prunet, and Frode Hansen. MASTER of the Cosmic Microwave Background Anisotropy Power Spectrum: A Fast Method for Statistical Analysis of Large and Complex Cosmic Microwave Background Data Sets. *ApJ*, 567(1):2–17, March 2002. doi:10.1086/338126.

W. Hu and S. Dodelson. Cosmic Microwave Background Anisotropies. *ARA&A*, 40:171–216, 2002.

D. Jeong, J. Chluba, L. Dai, M. Kamionkowski, and X. Wang. Effect of aberration on partial-sky measurements of the cosmic microwave background temperature power spectrum. *PhRvD*, 89(2):023003, January 2014. doi:10.1103/PhysRevD.89.023003.

Julien Lesgourgues. The Cosmic Linear Anisotropy Solving System (CLASS) I: Overview. *arXiv e-prints*, art. arXiv:1104.2932, April 2011. doi:10.48550/arXiv.1104.2932.

A. Lewis and S. Bridle. Cosmological parameters from CMB and other data: A Monte Carlo approach. *PhRvD*, 66(10):103511–+, November 2002.

M. Lueker, C. L. Reichardt, K. K. Schaffer, O. Zahn, P. A. R. Ade, K. A. Aird, B. A. Benson, L. E. Bleem, J. E. Carlstrom, C. L. Chang, H.-M. Cho, T. M. Crawford, A. T. Crites, T. de Haan, M. A. Dobbs, E. M. George, N. R. Hall, N. W. Halverson, G. P. Holder, W. L. Holzapfel, J. D. Hrubes, M. Joy, R. Keisler, L. Knox, A. T. Lee, E. M. Leitch, J. J. McMahon, J. Mehl, S. S. Meyer, J. J. Mohr, T. E. Montroy, S. Padin, T. Plagge, C. Pryke, J. E. Ruhl, L. Shaw, E. Shirokoff, H. G. Spieler, B. Stalder, Z. Staniszewski, A. A. Stark,

K. Vanderlinde, J. D. Vieira, and R. Williamson. Measurements of Secondary Cosmic Microwave Background Anisotropies with the South Pole Telescope. *ApJ*, 719:1045–1066, August 2010. doi:10.1088/0004-637X/719/2/1045.

A. Manzotti, W. Hu, and A. Benoit-Lévy. Super-sample CMB lensing. *PhRvD*, 90(2):023003, July 2014. doi:10.1103/PhysRevD.90.023003.

Planck Collaboration, R. Adam, P. A. R. Ade, N. Aghanim, M. Arnaud, J. Aumont, C. Baccigalupi, A. J. Banday, R. B. Barreiro, J. G. Bartlett, N. Bartolo, E. Battaner, K. Benabed, A. Benoit-Lévy, J. P. Bernard, M. Bersanelli, P. Bielewicz, A. Bonaldi, L. Bonavera, J. R. Bond, J. Borrill, F. R. Bouchet, F. Boulanger, A. Bracco, M. Bucher, C. Burigana, R. C. Butler, E. Calabrese, J. F. Cardoso, A. Catalano, A. Challinor, A. Chamballu, R. R. Chary, H. C. Chiang, P. R. Christensen, D. L. Clements, S. Colombi, L. P. L. Colombo, C. Combet, F. Couchot, A. Coulais, B. P. Crill, A. Curto, F. Cuttaia, L. Danese, R. D. Davies, R. J. Davis, P. de Bernardis, G. de Zotti, J. Delabrouille, J. M. Delouis, F. X. Désert, C. Dickinson, J. M. Diego, K. Dolag, H. Dole, S. Donzelli, O. Doré, M. Douspis, A. Ducout, J. Dunkley, X. Dupac, G. Efstathiou, F. Elsner, T. A. Enßlin, H. K. Eriksen, E. Falgarone, F. Finelli, O. Forni, M. Frailis, A. A. Fraisse, E. Franceschi, A. Frejsel, S. Galeotta, S. Galli, K. Ganga, T. Ghosh, M. Giard, Y. Giraud-Héraud, E. Gjerløw, J. González-Nuevo, K. M. Górski, S. Gratton, A. Gregorio, A. Gruppuso, V. Guillet, F. K. Hansen, D. Hanson, D. L. Harrison, G. Helou, S. Henrot-Versillé, C. Hernández-Monteagudo, D. Herranz, E. Hivon, M. Hobson, W. A. Holmes, K. M. Huffenberger, G. Hurier, A. H. Jaffe, T. R. Jaffe, J. Jewell, W. C. Jones, M. Juvela, E. Keihänen, R. Keskitalo, T. S. Kisner, R. Kneissl, J. Knoche, L. Knox, N. Krachmalnicoff, M. Kunz, H. Kurki-Suonio, G. Lagache, J. M. Lamarre, A. Lasenby, M. Lattanzi, C. R. Lawrence, J. P. Leahy, R. Leonardi, J. Lesgourgues, F. Levrier, M. Liguori, P. B. Lilje, M. Linden-Vørnle, M. López-Caniego, P. M. Lubin, J. F. Macías-Pérez, B. Maffei, D. Maino, N. Mandolesi, A. Mangilli, M. Maris, P. G. Martin, E. Martínez-González, S. Masi, S. Matarrese, P. Mazzotta, P. R. Meinhold, A. Melchiorri, L. Mendes, A. Mennella, M. Migliaccio, S. Mitra, M. A. Miville-Deschênes, A. Moneti, L. Montier, G. Morgante, D. Mortlock, A. Moss, D. Munshi, J. A. Murphy, P. Naselsky, F. Nati, P. Natoli, C. B. Netterfield, H. U. Nørgaard-Nielsen, F. Noviello, D. Novikov, I. Novikov, L. Pagano, F. Pajot, R. Paladini, D. Paoletti, B. Partridge, F. Pasian, G. Patanchon, T. J. Pearson, O. Perdereau, L. Perotto, F. Perrotta, V. Pettorino, F. Piacentini, M. Piat, E. Pierpaoli, D. Pietrobon, S. Plaszczynski, E. Pointecouteau, G. Polenta, N. Ponthieu, L. Popa, G. W. Pratt, S. Prunet, J. L. Puget, J. P. Rachen, W. T. Reach, R. Rebolo, M. Remazeilles, C. Renault, A. Renzi, S. Ricciardi, I. Ristorcelli, G. Rocha, C. Rosset, M. Rossetti, G. Roudier, B. Rouillé d'Orfeuil, J. A. Rubiño-Martín, B. Rusholme, M. Sandri, D. Santos, M. Savelainen, G. Savini, D. Scott, J. D. Soler, L. D. Spencer, V. Stolyarov, R. Stompor, R. Sudiwala, R. Sunyaev, D. Sutton, A. S. Suur-Uski, J. F. Sygnet, J. A. Tauber, L. Terenzi, L. Toffolatti, M. Tomasi, M. Tristram, M. Tucci, J. Tuovinen, L. Valenziano, J. Valiviita, B. Van Tent, L. Vibert, P. Vielva, F. Villa, L. A. Wade, B. D. Wandelt, R. Watson, I. K. Wehus, M. White, S. D. M. White, D. Yvon, A. Zacchei, and A. Zonca. Planck intermediate results. XXX. The angular power

spectrum of polarized dust emission at intermediate and high Galactic latitudes. *A&A*, 586:A133, February 2016. doi:10.1051/0004-6361/201425034.

Planck Collaboration, N. Aghanim, Y. Akrami, M. Ashdown, J. Aumont, C. Baccigalupi, M. Ballardini, A. J. Banday, R. B. Barreiro, N. Bartolo, S. Basak, R. Battye, K. Benabed, J. P. Bernard, M. Bersanelli, P. Bielewicz, J. J. Bock, J. R. Bond, J. Borrill, F. R. Bouchet, F. Boulanger, M. Bucher, C. Burigana, R. C. Butler, E. Calabrese, J. F. Cardoso, J. Carron, A. Challinor, H. C. Chiang, J. Chluba, L. P. L. Colombo, C. Combet, D. Contreras, B. P. Crill, F. Cuttaia, P. de Bernardis, G. de Zotti, J. Delabrouille, J. M. Delouis, E. Di Valentino, J. M. Diego, O. Doré, M. Douspis, A. Ducout, X. Dupac, S. Dusini, G. Efstathiou, F. Elsner, T. A. Enßlin, H. K. Eriksen, Y. Fantaye, M. Farhang, J. Fergusson, R. Fernandez-Cobos, F. Finelli, F. Forastieri, M. Frailis, A. A. Fraisse, E. Franceschi, A. Frolov, S. Galeotta, S. Galli, K. Ganga, R. T. Génova-Santos, M. Gerbino, T. Ghosh, J. González-Nuevo, K. M. Górski, S. Gratton, A. Gruppuso, J. E. Gudmundsson, J. Hamann, W. Handley, F. K. Hansen, D. Herranz, S. R. Hildebrandt, E. Hivon, Z. Huang, A. H. Jaffe, W. C. Jones, A. Karakci, E. Keihänen, R. Keskitalo, K. Kiiveri, J. Kim, T. S. Kisner, L. Knox, N. Krachmalnicoff, M. Kunz, H. Kurki-Suonio, G. Lagache, J. M. Lamarre, A. Lasenby, M. Lattanzi, C. R. Lawrence, M. Le Jeune, P. Lemos, J. Lesgourgues, F. Levrier, A. Lewis, M. Liguori, P. B. Lilje, M. Lilley, V. Lindholm, M. López-Caniego, P. M. Lubin, Y. Z. Ma, J. F. Macías-Pérez, G. Maggio, D. Maino, N. Mandolesi, A. Mangilli, A. Marcos-Caballero, M. Maris, P. G. Martin, M. Martinelli, E. Martínez-González, S. Matarrese, N. Mauri, J. D. McEwen, P. R. Meinhold, A. Melchiorri, A. Mennella, M. Migliaccio, M. Millea, S. Mitra, M. A. Miville-Deschênes, D. Molinari, L. Montier, G. Morgante, A. Moss, P. Natoli, H. U. Nørgaard-Nielsen, L. Pagano, D. Paoletti, B. Partridge, G. Patanchon, H. V. Peiris, F. Perrotta, V. Pettorino, F. Piacentini, L. Polastri, G. Polenta, J. L. Puget, J. P. Rachen, M. Reinecke, M. Remazeilles, A. Renzi, G. Rocha, C. Rosset, G. Roudier, J. A. Rubiño-Martín, B. Ruiz-Granados, L. Salvati, M. Sandri, M. Savelainen, D. Scott, E. P. S. Shellard, C. Sirignano, G. Sirri, L. D. Spencer, R. Sunyaev, A. S. Suur-Uski, J. A. Tauber, D. Tavagnacco, M. Tenti, L. Toffolatti, M. Tomasi, T. Trombetti, L. Valenziano, J. Valiviita, B. Van Tent, L. Vibert, P. Vielva, F. Villa, N. Vittorio, B. D. Wand elt, I. K. Wehus, M. White, S. D. M. White, A. Zacchei, and A. Zonca. Planck 2018 results. VI. Cosmological parameters. *A&A*, 641:A6, September 2020. doi:10.1051/0004-6361/201833910.

G. Polenta, D. Marinucci, A. Balbi, P. de Bernardis, E. Hivon, S. Masi, P. Natoli, and N. Vittorio. Unbiased estimation of an angular power spectrum. *JCAP*, 11:1–+, November 2005. doi:10.1088/1475-7516/2005/11/001.

L. D. Shaw, D. Nagai, S. Bhattacharya, and E. T. Lau. Impact of Cluster Physics on the Sunyaev-Zel'dovich Power Spectrum. *ApJ*, 725:1452–1465, December 2010. doi:10.1088/0004-637X/725/2/1452.

Simons Observatory Collaboration. The Simons Observatory: science goals and forecasts. *JCAP*, 2019(2):056, Feb 2019. doi:10.1088/1475-7516/2019/02/056.

Alessio Spurio Mancini, Davide Piras, Justin Alsing, Benjamin Joachimi, and Michael P. Hobson. COSMOPOWER: emulating cosmological power spectra for accelerated Bayesian inference from next-generation surveys. *MNRAS*, 511(2):1771–1788, April 2022. doi:10.1093/mnras/stac064.

Jesús Torrado and Antony Lewis. Cobaya: code for Bayesian analysis of hierarchical physical models. *JCAP*, 2021(5):057, May 2021. doi:10.1088/1475-7516/2021/05/057.

M. Tristram, J. F. Macías-Pérez, C. Renault, and D. Santos. XSPECT, estimation of the angular power spectrum by computing cross-power spectra with analytical error bars. *MNRAS*, 358:833–842, April 2005. doi:10.1111/j.1365-2966.2005.08760.x.

Licia Verde, Nils Schöneberg, and Héctor Gil-Marín. A tale of many H_0. *arXiv e-prints*, art. arXiv:2311.13305, November 2023. doi:10.48550/arXiv.2311.13305.

Matias Zaldarriaga. Nature of the E-B decomposition of CMB polarization. *PhRvD*, 64(10): 103001, November 2001. doi:10.1103/PhysRevD.64.103001.